J. Mech. Phys. Solids Vol. 36, No. 1, pp. 77–117, 1988.
Printed in Great Britain.

0022–5096/88 $3.00+0.00
Pergamon Press plc

A FINITE ELEMENT ANALYSIS OF SMALL-SCALE YIELDING NEAR A STATIONARY CRACK UNDER PLANE STRESS

R. NARASIMHAN and A. J. ROSAKIS

Division of Engineering and Applied Science, California Institute of Technology, Pasadena, CA 91125, U.S.A.

(*Received* 12 *December* 1986)

ABSTRACT

A DETAILED finite element analysis of the monotonic loading of a stationary crack is performed under Mode I plane stress, small-scale yielding conditions. A small strain, J_2 incremental plasticity theory is employed and both elastic-perfectly plastic and power law hardening materials are considered. Some issues such as the range of dominance of the asymptotic stress and deformation fields and the amount of non-proportional loading near the crack tip, which have received wide attention in the analogous plane strain problem, are examined. Special attention is devoted to the perfectly plastic idealization by performing a separate singular finite element analysis to clarify some details about the asymptotic stress and deformation fields. The full-field numerical solution is used to simulate synthetic (optical) caustic patterns at different distances from the tip, which are compared with experimental observations and with asymptotic analytical results.

1. INTRODUCTION

THE STRESS INTENSITY factor is a measure of the intensity of the stress and strain fields near a crack tip in linear elastic fracture mechanics. However, fracture in most structural materials, particularly low and intermediate strength metals, is often accompanied by plastic flow near the crack tip, invalidating the assumptions of linear elasticity theory. Under certain circumstances, the stress intensity factor can still be used to characterize the onset of crack growth, provided that the plastic zone is contained well within the region of dominance of the singular elastic field. This situation is often referred to as "small-scale yielding." But when plastic flow takes place over large size scales, one is compelled to seek continuum solutions for crack problems within the context of an elastic–plastic theory.

HUTCHINSON (1968a, b) and RICE and ROSENGREN (1968) performed the asymptotic analysis for stress and deformation fields near a monotonically loaded stationary crack tip in a power law hardening material obeying a deformation plasticity theory. The fact that the value of the J integral (RICE, 1968a) provides a measure of the intensity of the near-tip field in this asymptotic solution has prompted some investigators (e.g., BEGLEY and LANDES, 1972) to propose a criterion for the onset of crack

growth based on the attainment of a critical value for J. This proposal has been complemented by a wide range of experimental data (e.g., LANDES and BEGLEY, 1972).

In order to characterize fracture initiation based on this single macroscopic parameter, it is imperative that the plastic singular fields of HUTCHINSON (1968a, b) and RICE and ROSENGREN (1968) should dominate over a length scale that is large as compared to the fracture process zone. In this region, microstructural processes such as void nucleation and growth, microcracking, etc. take place. The fracture process zone is often believed to coincide with the region near the tip, wherein finite strain effects are significant. In addition to the above issues, another important factor that has to be considered is the possibility of non-proportional loading near the tip, which would render the deformation plasticity theory (on which the analysis of HUTCHINSON (1968a, b) and RICE and ROSENGREN (1968) is based) to be physically inappropriate.

The above issues have been examined by several investigators through numerical methods predominantly under the tensile plane strain mode of fracture. Accurate finite element studies with crack tip elements making use of special interpolation functions to account for the plastic strain singularity were conducted by LEVY, MARCAL, OSTERGREN and RICE (1971) and RICE and TRACEY (1973) for the perfectly plastic case and by TRACEY (1976) for hardening materials. These studies modelled Mode I plane strain, small-scale yielding conditions and employed an incremental plasticity theory. They confirmed the validity of the dominant fields of HUTCHINSON (1968a, b) and RICE and ROSENGREN (1968) in a region quite close to the crack tip. MCMEEKING (1977) performed a finite element calculation to model crack tip blunting based on a finite strain incremental plasticity theory under plane strain, small-scale yielding conditions. He observed that finite strain effects become important only for distances from the tip of the order of two or three times the crack opening displacement δ_t (which will be defined in Section 4). Strong path dependence of the J integral was also noticed within this region.

SHIH and GERMAN (1981) investigated the range of dominance of the plastic singular fields for a wide variety of specimen configurations and material properties from contained yielding to fully plastic conditions. They employed a small strain incremental plasticity theory and confined their attention to Mode I plane strain. MCMEEKING and PARKS (1979) also investigated configuration dependence within the context of a finite strain theory similar to that employed by MCMEEKING (1977) under large scale yielding. Thus, substantial work under Mode I plane strain conditions has been performed to provide a better understanding of the mechanics of crack tip state and also to specify size requirements for specimens used in fracture toughness testing to ensure J dominance.

However, very little information is available in the literature pertaining to the above issues under Mode I plane stress, despite its practical importance to structural problems. A preliminary numerical investigation was carried out by HILTON and HUTCHINSON (1971) under plane stress, small- (and large-) scale yielding conditions in which the plastic singular fields were imposed in a small circle near the crack tip. The value of J or some other equivalent plastic intensity factor was determined along with the nodal displacements from the finite element solution. SHIH (1973) applied their method to study combined Mode I and Mode II fracture problems under both plane strain and plane stress. Both these studies employed a deformation plasticity

theory and considered power-hardening materials. Also, the validity of the asymptotic solution of HUTCHINSON (1968a, b) and RICE and ROSENGREN (1968) was assumed over a length scale, which was not known *a priori*, although this was contained well within the plastic zone in these numerical simulations.

Some of the issues mentioned above, pertaining to the range of dominance of the asymptotic fields and the amount of non-proportional loading near the tip, which have received considerable attention in the plane strain problem, have not been examined in plane stress. Thus, detailed numerical work along the lines of RICE and TRACEY (1973), MCMEEKING (1977) and SHIH and GERMAN (1981) is required to firmly establish a conceptual understanding of fracture under plane stress conditions. This is usually more complex than in plane strain, primarily because the equations of plane stress plasticity are somewhat more involved (e.g., HILL, 1983).

In addition to the above considerations, a detailed numerical study of plane stress fracture is important because of the possibility of a direct comparison with optical experimental methods such as the method of caustics. This method, which has been employed to determine the stress intensity factor in linear elastic fracture problems (e.g., THEOCARIS and GDOUTOS, 1972), has recently been extended to applications in ductile fracture (ROSAKIS, MA and FREUND, 1983; ROSAKIS and FREUND, 1982). A knowledge of the range of dominance of the plastic singular fields is of primary importance to facilitate a proper interpretation of experimental data (ZEHNDER, ROSAKIS and NARASIMHAN, 1986). Also, information from full-field numerical solutions would be crucial in analysing the caustics obtained in regions outside the range of dominance of any particular asymptotic field.

In this work, an elaborate finite element investigation, with a very fine mesh elucidating the details near the crack tip, is undertaken to simulate Mode I plane stress, small-scale yielding conditions. No attempt has been made in this part of the work to incorporate the expected singularity in the strains by using special crack tip elements. Computations have been performed for materials obeying an incremental plasticity theory with no hardening and with a power-law hardening. In Section 2, the numerical formulation, finite element scheme, etc. are outlined. In Section 3, stationary crack tip fields under plane stress are reviewed. In Section 4, detailed results are presented for the plastic zones, stress and strain distributions, and crack opening displacement. Also, the path independence of the J integral is examined.

In Section 5, caustic patterns are simulated from the numerical solution at a wide range of distances from the crack tip and are compared with experimental observations (ZEHNDER *et al.*, 1986) and asymptotic results (ROSAKIS *et al.*, 1983). In Section 6, an additional numerical analysis, employing singular elements near the crack tip, is performed for the perfectly plastic case in order to examine the asymptotic stress and deformation fields. The issue of sensitivity of the numerical results to the near-tip mesh design is thus investigated. It is found that the dominant strain field near the tip for perfect plasticity is completely different from the limit of the singular solution of HUTCHINSON (1968a, b) and RICE and ROSENGREN (1968) for materials with low hardening. On the other hand, the numerical results for the near-tip stress field are in good agreement with the slip line solution of HUTCHINSON (1968b). In the light of this observation, it is suggested that the configuration dependence of crack tip deformation should be investigated under plane stress in the spirit of SHIH and GERMAN (1981)

and MCMEEKING and PARKS (1979). Such an analysis could be complemented by experimental results based on caustics.

2. NUMERICAL ANALYSIS

Formulation

The Mode I plane stress, small-scale yielding problem (RICE, 1968b) was modelled by considering a crack in a domain R, which was entirely represented by finite elements as shown in Figs. 1(a) and (b). Only the upper half-plane was considered because of Mode I symmetry. All field quantities are referred to with respect to an orthonormal frame $\{\mathbf{e}_1, \mathbf{e}_2, \mathbf{e}_3\}$ centered at the crack tip. The leading term in the displacements of the linear elastic asymptotic solution,

$$u_\alpha = K_I \sqrt{\frac{r}{2\pi}}\, \hat{u}_\alpha(\theta), \tag{2.1}$$

was specified as boundary conditions on the outermost boundary S of the domain.† The loading was applied through the Mode I stress intensity factor K_I, which occurs as an amplitude factor in equation (2.1).

The maximum extent of the plastic zone surrounding the crack tip was at all times within $\frac{1}{30}$ of the radius of the outermost contour S, so that the small-scale yielding condition was preserved. All plastic deformation was confined within the active region shown in Fig. 1(a), which has a total of 1704 four-noded elements and 3549 degrees of freedom. The large region surrounding this active mesh has a total of 40 rings with 56 elements in each ring and remained elastic throughout the entire computation. The constant stiffness of this region was statically condensed using a ring-by-ring static condensation procedure that involved a partial forward Gauss reduction at each stage.

The cutout in Fig. 1(a) is a fine mesh region near the crack tip, which is shown in detail in Fig. 1(b). This mesh was designed to have small rectangular elements parallel to the crack plane instead of being focused at the crack tip. No attempt has been made to incorporate the singularity of the plastic strains by using special crack tip elements in this analysis (see Section 6 and RICE and TRACEY, 1973). This was because the stress and strain fields at the end of the stationary load history were used as initial conditions for simulating stable crack extension, which will be reported elsewhere. The radius R_A of the active mesh and the radius of the outermost boundary S are about 385 times and 3400 times the size L of the smallest element near the crack tip, respectively.

The Mode I symmetry conditions that are given by

$$\left.\begin{aligned} \sigma_{12}(x_1, x_2 = 0) &= 0 \\ u_2(x_1, x_2 = 0) &= 0 \end{aligned}\right\}, \quad x_1 \geqslant 0, \tag{2.2}$$

† Throughout this paper, Greek subscripts will have the range 1, 2, while Latin subscripts will take values 1, 2, 3.

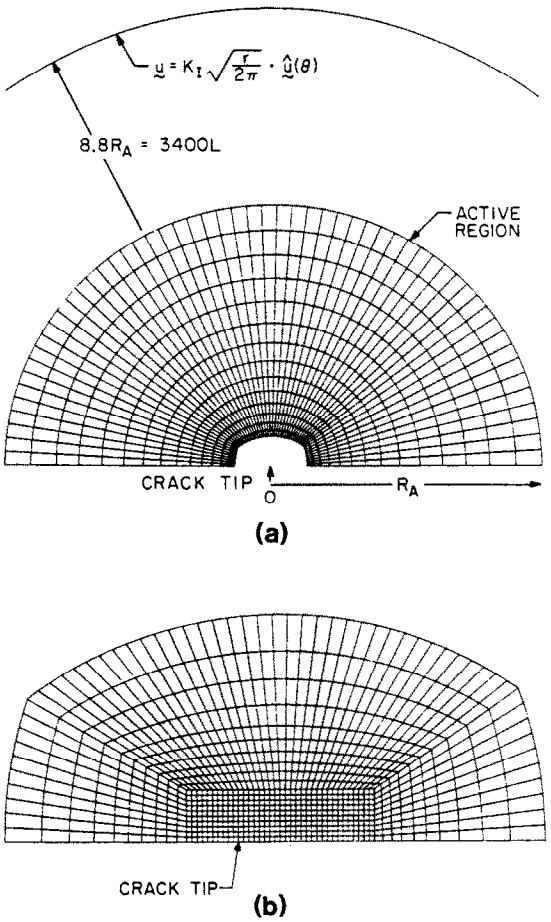

FIG. 1. Finite element mesh: (a) outer mesh; (b) fine mesh near the crack tip.

were imposed by attaching stiff springs in the x_2 direction to the nodes ahead of the crack tip. Traction-free conditions were imposed on the crackflank.

The type of element used was the four noded isoparametric quadrilateral, which was formed from four constant strain triangles with static condensation of the internal node. This element was suggested by NAGTEGAAL, PARKS and RICE (1974) to relieve artificial mesh-locking effects that occur under nearly incompressible conditions in plane strain. However, this problem does not arise in plane stress because there is a non-zero out-of-plane strain component ε_{33}, which is determined in terms of the in-plane strain components $\varepsilon_{\alpha\beta}$.

Material idealization

The materials that were numerically modelled were the elastic–perfectly plastic solids and isotropic power-hardening solids. A small strain incremental plasticity

theory was employed along with the Huber-Von Mises yield condition and the associated flow rule. The Huber-Von Mises yield condition for isotropic hardening takes the form,

$$f(\boldsymbol{\sigma}, \bar{\varepsilon}^p) = F(\boldsymbol{\sigma}) - \bar{\sigma}^2(\bar{\varepsilon}^p), \tag{2.3}$$

where $F(\boldsymbol{\sigma}) = \frac{3}{2}\mathbf{S}\cdot\mathbf{S}$ and $\bar{\varepsilon}^p = \int(\frac{2}{3}\dot{\varepsilon}_{ij}^p\dot{\varepsilon}_{ij}^p)^{1/2}\,dt$ is the accumulated equivalent plastic strain. In the above, $\mathbf{S}$ is the deviatoric stress tensor and $\bar{\sigma}(\bar{\varepsilon}^p)$ is defined by the following power hardening rule:

$$\frac{\bar{\varepsilon}^p}{\varepsilon_0} = \left(\frac{\bar{\sigma}}{\sigma_0}\right)^n - \frac{\bar{\sigma}}{\sigma_0}. \tag{2.4}$$

For the elastic–perfectly plastic case, $\bar{\sigma}$ takes the constant value of σ_0, the yield stress in uniaxial tension. In equation (2.4), ε_0 is the yield strain in uniaxial tension.

Within the context of the small strain flow theory of plasticity, the total strain rate tensor can be decomposed into elastic and plastic parts:

$$\dot{\boldsymbol{\varepsilon}} = \dot{\boldsymbol{\varepsilon}}^e + \dot{\boldsymbol{\varepsilon}}^p. \tag{2.5}$$

The stress rate tensor $\dot{\boldsymbol{\sigma}}$ is related to the elastic strain rate tensor $\dot{\boldsymbol{\varepsilon}}^e$ through a constant, isotropic, positive definite elasticity tensor $\mathbf{C}$ as

$$\dot{\boldsymbol{\sigma}} = \mathbf{C}\dot{\boldsymbol{\varepsilon}}^e. \tag{2.6}$$

The plastic strain rate tensor $\dot{\varepsilon}^p$ is normal to the yield surface and the flow rule takes the form

$$\dot{\boldsymbol{\varepsilon}}^p = \frac{\dot{\lambda}}{3}F_{\boldsymbol{\sigma}} = \dot{\lambda}\mathbf{S}, \tag{2.7}$$

where $\dot{\lambda} \geqslant 0$.

By using equations (2.3)–(2.7) the constitutive law for material currently experiencing elastic–plastic deformation can be obtained as

$$\dot{\sigma}_{ij} = C^*_{ijkl}\dot{\varepsilon}_{kl} = \left[C_{ijkl} - \frac{C_{ijpq}S_{pq}S_{mn}C_{mnkl}}{S_{rt}C_{rtuv}S_{uv} + \frac{4}{9}\bar{\sigma}^2 H}\right]\dot{\varepsilon}_{kl}. \tag{2.8}$$

In the above, $H = d\bar{\sigma}/d\bar{\varepsilon}^p$ and can be obtained from (2.4) for hardening solids and is set equal to zero for perfect plasticity.

In the present analysis, (2.3) and (2.8) were used along with the plane stress constraint, which requires

$$\sigma_{3i} \equiv 0. \tag{2.9}$$

By using (2.9) in (2.8), an expression for $\dot{\varepsilon}_{33}$ can be obtained in terms of $\dot{\varepsilon}_{\alpha\beta}$.

Finite element scheme

A displacement based finite element method was employed in the analysis. The finite element equations were derived from the principle of virtual work. At a time $(t+\Delta t)$ this takes the form

$$\int_R \boldsymbol{\sigma}(t+\Delta t)\cdot\delta\boldsymbol{\varepsilon}\,\mathrm{d}A = \int_{\partial R} \mathbf{T}(t+\Delta t)\cdot\delta\mathbf{u}\,\mathrm{d}s. \tag{2.10}$$

Here $\boldsymbol{\sigma}(t+\Delta t)$ represents the Cauchy stress tensor, which satisfies equilibrium at time $(t+\Delta t)$ and $\mathbf{T}(t+\Delta t)$ the imposed traction vector on the boundary ∂R. Also, $\delta\mathbf{u}$ represents the virtual displacement vector that vanishes on the part of the boundary where the displacements are specified and $\delta\boldsymbol{\varepsilon}$ is the associated small strain tensor.

After linearizing about the equilibrium configuration at time t and introducing the finite element approximation, the following incremental equilibrium equations are obtained in matrix form (e.g., BATHE, 1982):

$$\mathbf{K}_T\Delta\mathbf{U} = \mathbf{F}(t+\Delta t)-\mathbf{P}(t). \tag{2.11}$$

Here $\Delta\mathbf{U} = \mathbf{U}(t+\Delta t)-\mathbf{U}(t)$ is the vector of nodal point displacement increments. Also, $\mathbf{K}_T = \int_R \mathbf{B}^T\mathbf{D}\mathbf{B}\,\mathrm{d}A$ is the tangent stiffness matrix corresponding to the configuration at time t, $\mathbf{B}$, the strain displacement matrix ($\boldsymbol{\varepsilon} = \mathbf{B}\mathbf{U}$) and $\mathbf{D}$, the material constitutive matrix. $\mathbf{D}$ will be equal to $\mathbf{C}$ for purely elastic response and $\mathbf{C}^*$ for elastic–plastic material response. $\mathbf{F}(t+\Delta t)$ is the vector of externally applied nodal point loads at time $(t+\Delta t)$ and $\mathbf{P}(t) = \int_R \mathbf{B}^T\boldsymbol{\sigma}(t)\,\mathrm{d}A$ is the vector of nodal point forces equivalent to the element stresses at time t.

In the present analysis, time is only a convenient variable that represents different levels of load intensities. An iterative Newton-Raphson procedure (e.g., BATHE and CIMENTO, 1980; BATHE, 1982) was employed in the solution of the incremental equilibrium equations (2.11). This method is summarized in the Appendix.

Stress computation

As was observed above, the finite element scheme solves the displacement equations of equilibrium in an incremental fashion. Hence, the constitutive laws presented earlier that deal with stress and strain rates were used approximately to relate small finite increments in stresses and strains. An explicit integration procedure also known as the Tangential Predictor-Radial Return method was employed to integrate the incremental stress–strain law. As shown by SCHREYER, KULAK and KRAMER (1979), this method, if used with subincrementation (as in the present analysis), is very accurate for plane stress conditions.

It is important to recall that the requirement of plane stress imposes a constraint for the out-of-plane strain increment $\Delta\varepsilon_{33}$ in terms of the in-plane strain increments $\Delta\varepsilon_{\alpha\beta}$. Due to this constraint, it is more convenient to perform computations with stress and strain tensors instead of with their deviatoric parts as is normally done in plane strain. The method of stress computation is outlined in the Appendix.

Solution strategy

As noted earlier, the loading was applied through the Mode I stress intensity factor K_I, which enters the far-field displacement boundary condition (2.1). An initial load step was performed in which K_I was small enough to ensure that all the elements remained elastic. K_I was then scaled to cause incipient yielding in the element nearest to the crack tip.

Subsequent load steps were performed by increasing K_I by 5–10% of the incipient value at a time and iterating for convergence to equilibrium. Each load step required typically 3–4 iterations before converging to an accepted equilibrium configuration. Yielding was continued till the plastic zone surrounding the crack tip had a maximum extent of about 50 or 100 times the smallest element size L in order to guarantee sufficient resolution near the crack tip.

3. STATIONARY CRACK TIP FIELDS

Power-hardening solids

HUTCHINSON (1968a, b) and RICE and ROSENGREN (1968) investigated the asymptotic stress and strain fields near a monotonically loaded stationary crack tip in an elastic–plastic solid. The dominant singular term of their analysis will be referred to as HRR in the sequel. In their work, a J_2 deformation plasticity theory and a power-law hardening idealization similar to (2.4) were assumed.

The HRR analysis employs a small strain formulation and assumes a separable form in polar coordinates r and θ, for the dominant term of the solution, to obtain

$$\left.\begin{aligned} \sigma_{ij} &\sim \sigma_0 \left[\frac{J}{\sigma_0 \varepsilon_0 I_n r}\right]^{1/n+1} \tilde{\sigma}_{ij}(\theta, n) \\ \varepsilon_{ij}^p &\sim \varepsilon_0 \left[\frac{J}{\sigma_0 \varepsilon_0 I_n r}\right]^{n/n+1} \tilde{\varepsilon}_{ij}^p(\theta, n) \end{aligned}\right\}, \quad r \to 0. \tag{3.1}$$

In (3.1), σ_0 and ε_0 are the yield stress and strain in uniaxial tension and n is the hardening exponent. The angular factors $\tilde{\sigma}_{ij}(\theta, n)$ and $\tilde{\varepsilon}_{ij}^p(\theta, n)$ depend on the mode of loading and on the hardening exponent. The dimensionless quantity I_n, which is defined in HUTCHINSON (1968a), decreases from 5 for $n = 1$ to about 2.6 for $n \to \infty$ under plane stress. J in (3.1) is the value of the J integral of RICE (1968a).

For plane deformations, the J integral is defined for any path of integration Γ by

$$J = \int_\Gamma (W \nu_1 - \nu_i \sigma_{ij} u_{j,1}) \, ds, \tag{3.2}$$

where W is the local stress work density, ν_i a unit vector normal to Γ and u_i is a particle displacement vector. For our purposes, Γ will denote an open contour surrounding the crack tip. The integral (3.2) has the well-known property of path independence for a wide class of solids, including materials that obey the deformation theory of plasticity. Under small-scale yielding conditions, J can be evaluated from contours taken in the far-field (K dominated) elastic region as,

$$J = \frac{K_I^2}{E} \tag{3.3}$$

for plane stress. It is important to note that J enters (3.1) as an amplitude factor and hence provides a unique measure for characterizing fracture initiation at the crack tip.

The main limitation of the HRR analysis is the unknown range of dominance (e.g., with respect to maximum extent of the plastic zone) of the singular solution. This issue is important since this range of dominance should be large as compared with the fracture process zone and the region near the crack tip where the small strain plasticity theory breaks down. From the experimental standpoint, this information is crucial in the proper interpretation of experimental data based on optical measurements (ZEHNDER *et al.*, 1986).

Also, the discrepancy between the deformation theory and the more appropriate incremental theory of plasticity has to be assessed from the context of crack tip fields. In addition, another serious limitation that will be pointed out later occurs when the limit $n \to \infty$ is taken. This is associated with the change in nature of the governing equations in the limit as the perfect plasticity case is approached.

The above issues will be investigated from the point of view of the plane stress full-field numerical solution presented here. This solution simulates small-scale yielding conditions and employs an incremental plasticity theory.

Perfectly plastic solids : stress field

For perfectly plastic solids, the following important assumptions regarding the asymptotic nature of the stress field are usually made :

$$\left.\begin{aligned} \sigma_{ij}(r,\theta) &\sim \sigma^{\circ}_{ij}(\theta) \\ \frac{\partial \sigma_{ij}(r,\theta)}{\partial \theta} &\sim \sigma'_{ij}(\theta) = \frac{d\sigma^{\circ}_{ij}}{d\theta} \\ r\frac{\partial \sigma_{ij}}{\partial r} &\sim o(1) \end{aligned}\right\}, \quad r \to 0. \tag{3.4}$$

It is important to bear in mind that the field equations for perfect plasticity may be hyperbolic,† while those for hardening solids are elliptic.

Equation (3.4) can be used to obtain asymptotic forms of equilibrium equations and the Von Mises yield condition (RICE and TRACEY, 1973). These can be employed to show that only two types of asymptotic plastic sectors can exist near the crack tip. These are as follows for plane stress.

(*i*) *Centered fan sector*

In this sector, radial lines are stress characteristics and the asymptotic stress field has the following form,

$$\left.\begin{aligned} \sigma^{\circ}_{rr}(\theta) &= \tau_0 \cos(\theta - \theta_0) \\ \sigma^{\circ}_{\theta\theta}(\theta) &= 2\tau_0 \cos(\theta - \theta_0) \\ \sigma^{\circ}_{r\theta}(\theta) &= \tau_0 \sin(\theta - \theta_0) \end{aligned}\right\}, \tag{3.5}$$

where θ_0 is an arbitrary constant angle and τ_0 is the yield stress in pure shear.

(*ii*) *Constant stress sector*

In this sector, the Cartesian components of the stresses are constant,

$$\sigma^{\circ}_{\alpha\beta}(\theta) = b_{\alpha\beta}. \tag{3.6}$$

† For perfectly plastic solids *under plane stress*, the governing equations for the stresses could be hyperbolic, parabolic or elliptic (e.g., HILL, 1983).

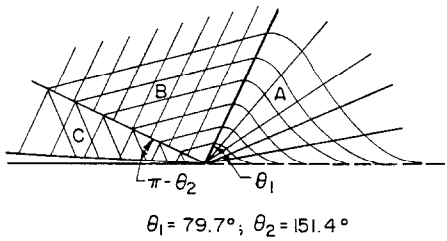

FIG. 2. Analytical asymptotic field near a stationary crack tip in a perfectly plastic solid under plane stress represented by stress characteristics.

The constants $b_{\alpha\beta}$ are related by the yield condition. Straight lines along which the direct components of the stress deviator $S^{\circ}_{\alpha\beta}$ vanish are stress characteristics (HILL, 1983).

HUTCHINSON (1968b) assembled a solution for the near-tip field comprising of a combination of the above sectors as shown in Fig. 2. The region marked A is a centered fan sector extending from $\theta = 0^{\circ}$ to $\theta = 79.7^{\circ}$, while the regions B and C are two constant stress sectors, which occupy the angles from $\theta = 79.7^{\circ}$ to $\theta = 180^{\circ}$. The stresses in Sector A are as given by (3.5) with $\theta_0 = 0$. In particular, it should be noted that the stresses ahead of the crack tip ($\theta = 0$) are given by

$$\sigma^{\circ}_{11} = \tau_0 \quad \sigma^{\circ}_{22} = 2\tau_0 \quad \sigma^{\circ}_{12} = 0. \tag{3.7}$$

There is also a discontinuity in the σ_{rr} stress component between the two constant stress sectors B and C, which is admissible as long as the crack remains stationary.

Perfectly plastic solids : deformation fields

As noted by RICE (1968a) in the case of plane strain, singularities in strains result when slip lines focus at a point as in centered fan sectors. The displacements u_i (or the rates $\dot{u}_i$ in a proper incremental formulation (HILL, 1983)) are functions of angle θ as the crack tip is approached within centered fan sectors resulting in a discrete crack opening displacement at the tip. The following assumptions are often made (RICE and TRACEY, 1973) about the displacements u_i (or the rates $\dot{u}_i$) within centered fan sectors,

$$\left.\begin{aligned} u_i(r,\theta) &\sim u_i^{\circ}(\theta) \\ \frac{\partial u_i(r,\theta)}{\partial\theta} &\sim u_i'(\theta) = \frac{du_i}{d\theta} \\ r\frac{\partial u_i}{\partial r} &\sim o(1) \end{aligned}\right\}, \quad r \to 0. \tag{3.8}$$

Since radial lines are stress characteristics in the fan, ε^p_{rr} is nonsingular while $\varepsilon^p_{\theta\theta}$ (or $\dot{\varepsilon}^p_{\theta\theta}$) and $\varepsilon^p_{r\theta}$ (or $\dot{\varepsilon}^p_{r\theta}$) are singular as $O(1/r)$ when the crack tip is approached within the fan. Thus, it is possible to write

$$\left.\begin{aligned} \varepsilon^p_{\theta\theta} &\sim \varepsilon_0 \frac{\hat{\varepsilon}^p_{\theta\theta}(\theta)}{r} \\ \varepsilon^p_{r\theta} &\sim \varepsilon_0 \frac{\hat{\varepsilon}^p_{r\theta}(\theta)}{r} \end{aligned}\right\}, \quad r \to 0 \tag{3.9}$$

within fan sectors. The angular factors $\hat{\varepsilon}^p_{\theta\theta}(\theta)$ and $\hat{\varepsilon}^p_{r\theta}(\theta)$ are *non-unique* and cannot be determined from a local analysis. They depend on a solution to the entire boundary value problem. However, from the flow rule,

$$\dot{\varepsilon}_{ij}^{p} = \left(\frac{\dot{\varepsilon}_{kl}^{p}\dot{\varepsilon}_{kl}^{p}}{2}\right)^{1/2} \frac{S_{ij}}{\tau_0}, \tag{3.10}$$

the following relation can be obtained between $\dot{\varepsilon}_{\theta\theta}^{p}$ and $\dot{\varepsilon}_{r\theta}^{p}$,

$$\dot{\varepsilon}_{r\theta}^{p} = \dot{\varepsilon}_{\theta\theta}^{p} \frac{S_{r\theta}}{S_{\theta\theta}}, \tag{3.11}$$

provided $S_{\theta\theta} \neq 0$. Although this equation strictly applies for the strain rates in an incremental theory, it can be used to relate the total strains if the stresses remained constant at a material point from the time it was enveloped by the plastic zone. Hence, it is expected to hold approximately between the asymptotic angular strain factors $\hat{\varepsilon}_{\theta\theta}^{p}(\theta)$ and $\hat{\varepsilon}_{r\theta}^{p}(\theta)$.

The dominant HRR solution for the stresses (3.1) approaches the limiting slipline distribution of perfect plasticity as the hardening exponent $n \to \infty$. But as has been observed by LEVY *et al.* (1971) and RICE and TRACEY (1973) for plane strain, one cannot in general expect the HRR singular solution for the strains as $n \to \infty$ to be the dominant solution for perfect plasticity because of the non-uniqueness noted earlier.

On the other hand, the strain components are (in general) non-singular in the constant stress sectors and the same displacement results if the crack tip is approached along different radial lines in these sectors.

An expression for the near-tip J integral can be obtained from the asymptotic form (3.9) following plane strain analysis of RICE (1968a). Taking the contour Γ in (3.2) to be a circle of radius r, one can write (3.2) as

$$J = r\int_{-\pi}^{\pi} \{W\cos\theta - \sigma_{rr}[\varepsilon_{rr}\cos\theta - (\varepsilon_{r\theta}-\omega)\sin\theta] - \sigma_{r\theta}[(\varepsilon_{r\theta}+\omega)\cos\theta - \varepsilon_{\theta\theta}\sin\theta]\}\,\mathrm{d}\theta. \tag{3.12}$$

In the above equation, ω is the rotation, and

$$\omega = -\varepsilon_{r\theta} + o\left(\frac{1}{r}\right), \quad r \to 0. \tag{3.13}$$

Also,

$$\left.\begin{aligned} \varepsilon_{rr} &= o\left(\frac{1}{r}\right) \\ W &= W^{p} + o\left(\frac{1}{r}\right) \end{aligned}\right\}, \quad r \to 0, \tag{3.14}$$

where

$$W^{p} = \int_0^{\varepsilon^{p}} \bar{\sigma}\,\mathrm{d}\bar{\varepsilon}^{p} = \sigma_0\bar{\varepsilon}^{p} \approx \sigma_0\left(\frac{2}{3}\varepsilon_{ij}^{p}\varepsilon_{ij}^{p}\right)^{1/2}.$$

Taking $r \to 0$ in (3.12) and using the asymptotic equations (3.5), (3.9), (3.13) and (3.14), one obtains

$$J_{\mathrm{tip}} = \left(\frac{2\sigma_0^2}{\sqrt{3}E}\right)\int_0^{\theta^*} \{2[(\hat{\varepsilon}_{r\theta}^{p})^2 + (\hat{\varepsilon}_{\theta\theta}^{p})^2]^{1/2}\cos\theta + \hat{\varepsilon}_{r\theta}^{p}\sin 2\theta + \hat{\varepsilon}_{\theta\theta}^{p}\sin^2\theta\}\,\mathrm{d}\theta, \tag{3.15}$$

where θ^* is the maximum angular extent of the fan.

4. RESULTS AND DISCUSSION

The computations were performed for two levels of power hardening, $n = 5$ and 9 and also for the elastic–perfectly plastic case, which is referred to as $n = \infty$ in the following discussion of the results. It should, however, be noted that the elastic–perfectly plastic calculation was performed with $H = d\bar{\sigma}/d\bar{\varepsilon}^p \equiv 0$ in the constitutive equation (2.8). The ratio of the Young's modulus to the yield stress in pure shear (E/τ_0) was taken as 1400 for the two cases of power-hardening and as 350 for the elastic–perfectly plastic calculation. The Poisson's ratio was taken as 0.3 for all cases.

Plastic zones

The plastic zone surrounding the crack tip is shown in Fig. 3 for the three values of hardening exponent n. The crack tip is situated at the origin of the coordinate axes that have been made dimensionless by the parameter $(K_I/\sigma_0)^2$. This parameter has the unit of length and also contains a measure of the far-field loading. Hence, the size of the plastic zone is expected to scale with respect to this parameter under small-scale yielding conditions. A point in the figure represents a yielded integration station within an element. It should be noted that the plastic zone becomes less rounded and spreads more ahead of the crack tip with decreasing hardening (increasing n).

These plastic zones agree well in shape but are slightly smaller in size as compared with the results of SHIH (1973), who employed a deformation plasticity theory and used a singular element near the crack tip. The maximum extent of the plastic zone that occurs ahead of the crack tip ($\theta = 0$) is about $r_p = 0.22(K_I/\sigma_0)^2$, $0.25(K_I/\sigma_0)^2$ and $0.29(K_I/\sigma_0)^2$ for $n = 5$, 9 and ∞, respectively. For comparison, Shih's calculation indicates an r_p of about $0.32(K_I/\sigma_0)^2$ for $n = 25$, and TADA, PARIS and IRWIN (1973) report $r_p = (1/\pi)(K_I/\sigma_0)^2$ for $n = \infty$ based on an approximate calculation. The slightly larger size of the plastic zone obtained by Shih could be due to the imposition of the HRR singular solution in a small circle around the crack tip in his analysis. The present computation introduces no such *a priori* constraint.

In Fig. 4 the numerically obtained plastic zone for $n = 9$ is compared with the visual evidence of permanent plastic deformation observed on the surface of a thin compact tension specimen (ZEHNDER *et al.*, 1986). The material used in this experiment was a 4340 carbon steel with a power-hardening exponent of 9 in uniaxial tension. The experimental and numerical plastic zones agree well in shape and also in size when the load levels in the experiment were small and there were no boundary interaction effects (contained yielding).

Radial distribution of stresses

The distribution of the normalized opening stress, σ_{22}/τ_0, along the x_1 axis ahead of the crack tip and within the plastic zone is shown in Fig. 5. The centroidal values of stress in the row of elements ahead of the crack tip have been used in making this plot. Advantage has again been taken of the self-similarity noted earlier, with the distance from the crack tip being measured in terms of the dimensionless variable $x_1/(K_I/\sigma_0)^2$. The finite element results agree to within 1% with the HRR asymptotic

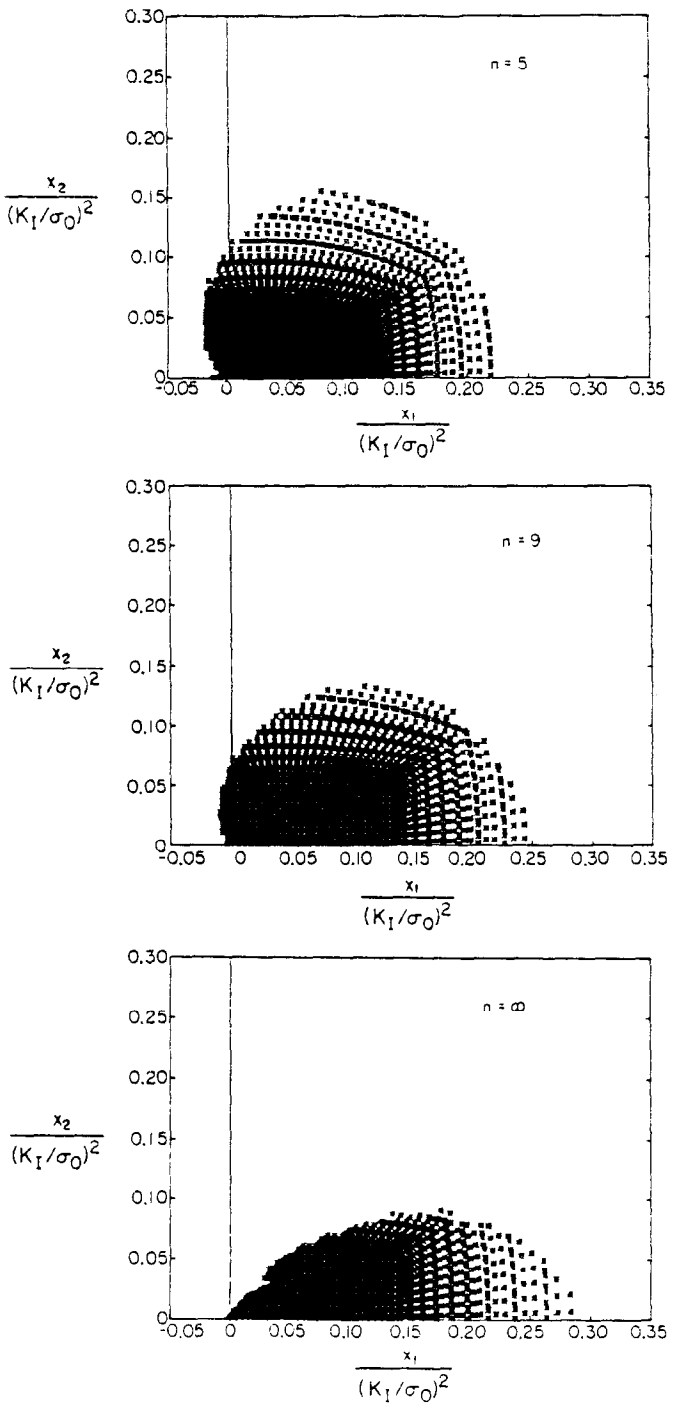

FIG. 3. Plastic zones surrounding the crack tip for three levels of hardening: $n = 5$, 9 and ∞.

stress distribution (3.1), which is shown by the solid lines in the figure, in the range $0 < x_1 < 0.08(K_I/\sigma_0)^2$. For example, at $x_1 = 0.018(K_I/\sigma_0)^2$, the ratio of the finite element to the HRR asymptotic stress is 3.13/3.14, 2.66/2.67 and 1.999/2.0 for $n = 5$, 9 and ∞, respectively.

The values given by the HRR distribution for σ_{22} are higher than their finite element counterparts by about 8% at the elastic–plastic boundary. This is in marked contrast to the corresponding result in plane strain (e.g., TRACEY, 1976), where strong deviation of the finite element solution from the HRR distribution was reported even for small distances from the crack tip. Also, it should be observed from Fig. 5 that there is only slight dependence of σ_{22} on n for $x_1 > 0.15(K_I/\sigma_0)^2$. The finite element values differ by less than 10% (with respect to n) in this range.

The radial variation of all the normalized stress components ahead of the crack tip within the plastic zone for the elastic–perfectly plastic case is shown in Fig. 6. The finite element values near the crack tip are in excellent agreement with the asymptotic slipline solution of HUTCHINSON (Fig. 2). At $x_1 = 0.01(K_I/\sigma_0)^2$, σ_{11} and σ_{22} are 0.98 τ_0 and 1.999 τ_0, respectively, which compares very closely with the values of τ_0 and $2\tau_0$ given by the slipline solution (equation (3.7)). Also, Fig. 6 indicates that the σ_{11} stress component has a strong radial variation ahead of the crack tip, with a value at the elastic–plastic boundary of about 1.40 τ_0. This suggests curving of the leading boundary of the fan at moderate distances from the tip.

The plane-stress Huber-Von Mises yield surface can be represented by an ellipse in principal stress space in the following parametric form (HILL, 1983):

$$\left.\begin{aligned} \sigma_1 &= 2\tau_0 \cos\left(\omega - \frac{\pi}{6}\right) \\ \sigma_2 &= 2\tau_0 \cos\left(\omega + \frac{\pi}{6}\right) \\ \omega &= \omega(r, \theta) \end{aligned}\right\}. \tag{4.1}$$

For $\sigma_1 \geqslant \sigma_2$, the angle ω varies in the range $0 \leqslant \omega \leqslant \pi$. The governing equations for the stresses are hyperbolic if $\pi/6 < \omega < 5\pi/6$, parabolic if $\omega = \pi/6$ or $5\pi/6$, and elliptic if $0 \leqslant \omega < \pi/6$ or $5\pi/6 < \omega \leqslant \pi$. The value of $\omega(r \to 0, 0)$ corresponding to the asymptotic stresses (3.7) is $\pi/6$, whereas the stresses at the elastic–plastic boundary ahead of the crack tip give $\omega(r_p, 0) \approx \pi/12$. Thus, while the stress state ahead of the crack is parabolic near the tip, it appears to be elliptic at the elastic–plastic boundary.

It is important from the viewpoint of optical experimental methods (such as caustics) to determine the effect of the crack tip plastic zone on the stress and deformation fields in the surrounding elastic region, in order to properly interpret the experimental data. To examine this effect, the radial distribution of stresses in the ray ahead of the crack tip is shown on an expanded scale in Fig. 7 for the two levels of hardening, $n = 5$ and 9. The stresses given by the singular elastic solution (K_I field) are shown for comparison by the solid line in the figure. It is found that the σ_{22} stress component obtained from the numerical solution is higher than that given by the singular elastic field at the elastic–plastic boundary ($r = r_p$) by more than 30%. However, the stress

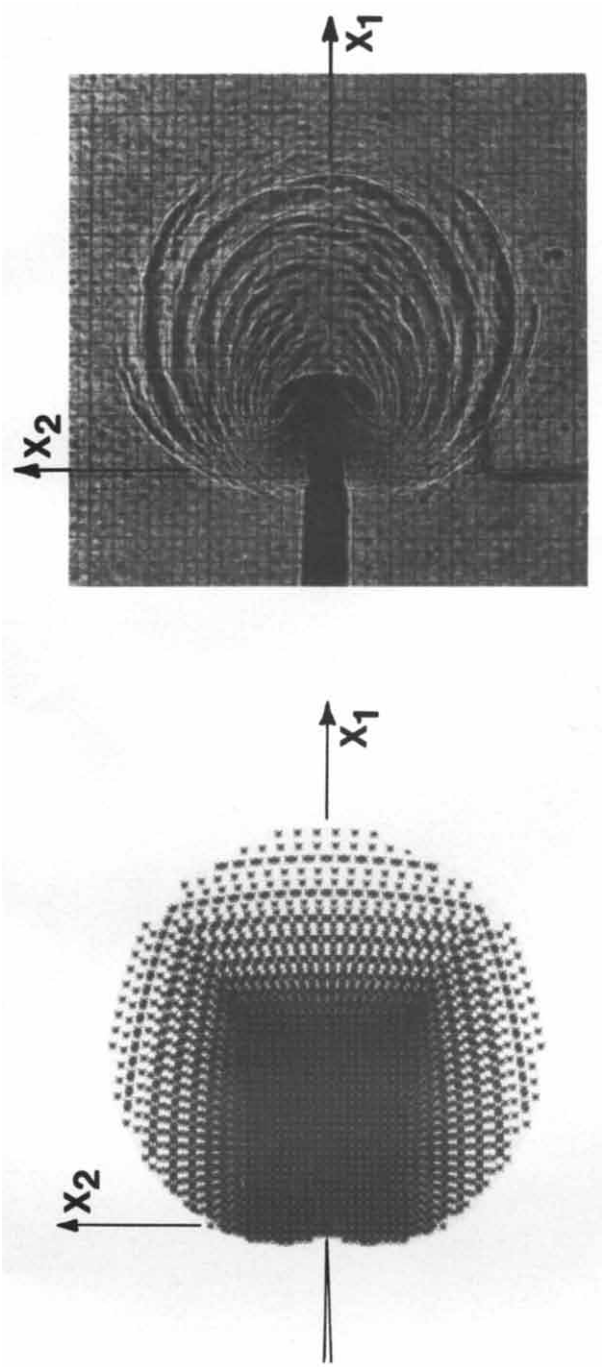

FIG. 4. Comparison of (a) numerical with (b) experimental plastic zones for material with $n = 9$.

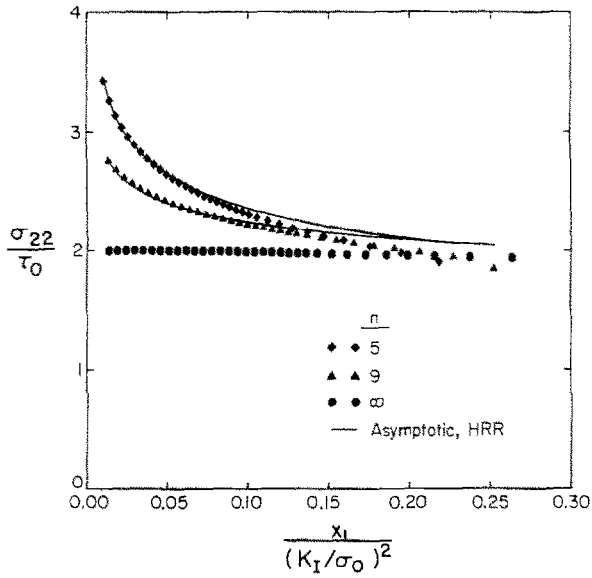

FIG. 5. Radial distribution of opening stress ahead of the crack tip. The solid lines represent the HRR asymptotic distribution.

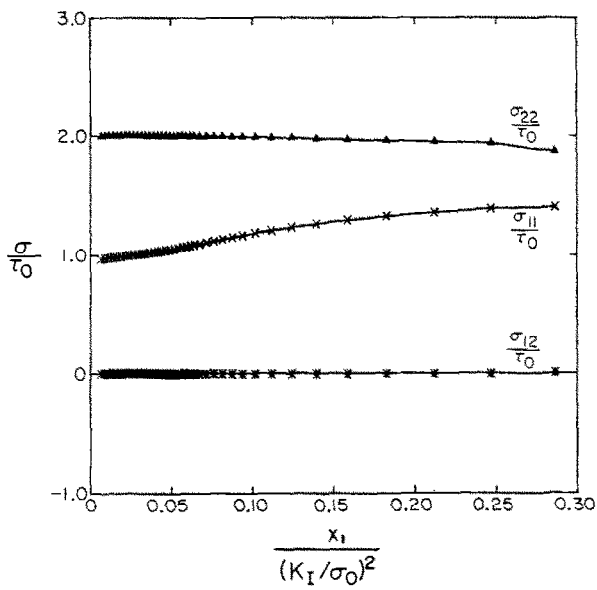

FIG. 6. Radial stress distribution ahead of the crack tip for the perfectly plastic case.

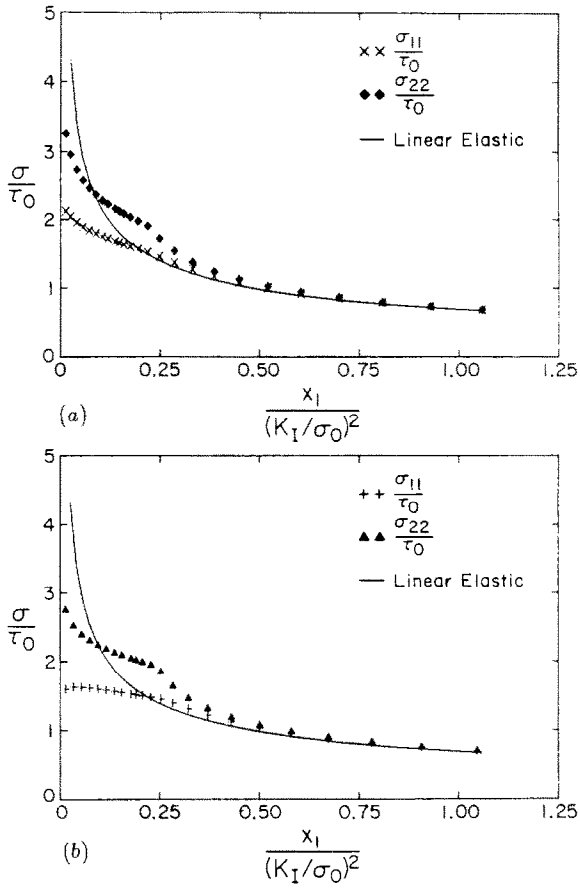

FIG. 7. Comparison of the radial stress distribution ahead of the tip as given by the K_I field (solid line) with the finite element solution for materials with (a) $n = 5$ and (b) $n = 9$.

distribution undergoes a rapid transition outside the plastic zone and differs from the K_I field by less than 8% for $r > 1.5r_p$. Also, the stress distribution in the surrounding elastic region seems to be quite insensitive to the hardening level.

Radial distribution of plastic strains

The radial variation of the normalized plastic strains $\varepsilon_{22}^p/\varepsilon_0$ and $\varepsilon_{33}^p/\varepsilon_0$ with respect to normalized distance ahead of the crack tip is shown in Fig. 8 for the two levels of power hardening. The HRR solution for the asymptotic strain distribution (equation (3.1)) is shown by the solid lines in the figure. The finite element solution, although slightly smaller than the HRR distribution near the crack tip, appears to indicate the correct singular behaviour in the range $r < 0.3r_p$. It should be recalled that a very detailed mesh was used near the crack tip (Fig. 1(b)), and that the plastic zone was quite large as compared with the smallest element size (at least 50 times) at the stage

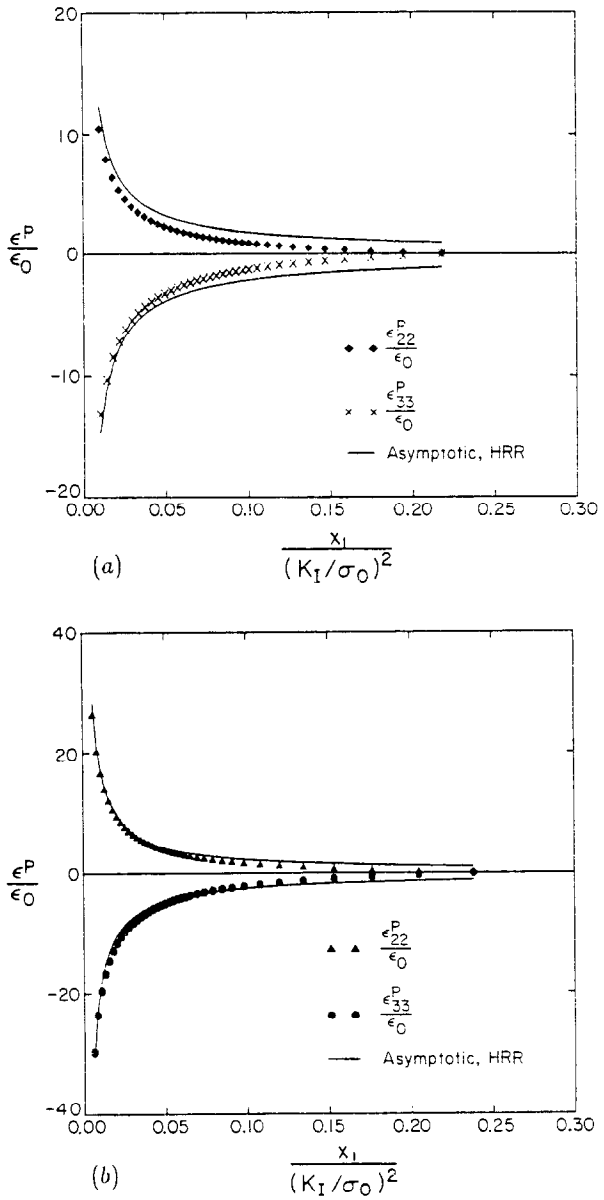

FIG. 8. Radial variation of the plastic strains ahead of the crack tip for materials with (a) $n = 5$ and (b) $n = 9$ and comparison with HRR solution (solid lines).

when these results were taken. These factors compensate to some extent for the incorrect modelling of the singularity (3.1) by our using linear shape functions for the crack tip elements.

The radial variation of the normalized plastic strains ahead of the crack tip for the elastic–perfectly plastic case is shown in Fig. 9. The solid line in the figure is the limit

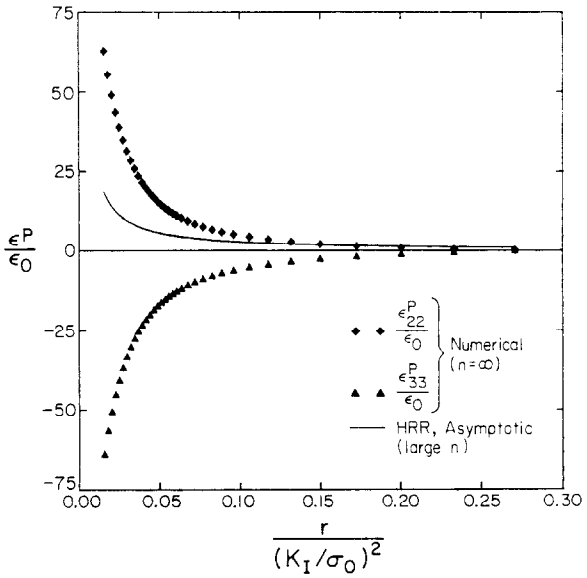

FIG. 9. Radial variation of plastic strains ahead of tip for perfectly plastic case. A vast discrepancy with the HRR singular solution for large n (SHIH, 1973; ROSAKIS *et al.*, 1983) is observed.

of the HRR dominant singular solution for $\varepsilon^p_{22}/\varepsilon_0$ for large n, which is given by (SHIH, 1973; ROSAKIS *et al.*, 1983),

$$\frac{\varepsilon^p_{22}}{\varepsilon_0}\Bigg|^{HRR}_{n\to\infty} \approx \frac{0.9\tilde{r}_p}{r}, \quad \theta = 0, \quad r \to 0, \tag{4.2}$$

where

$$\tilde{r}_p = \frac{1}{\pi}\left(\frac{K_I}{\sigma_0}\right)^2.$$

The finite element solution for the strains seems to indicate the correct $1/r$ variation near the crack tip ($r < 0.04(K_I/\sigma_0)^2$) but is about 3.3 times the values given by (4.2).

As has already been noted in Section 3, the HRR singular strain solution as $n \to \infty$, cannot (in general) be expected to provide the dominant solution for perfect plasticity because of the non-uniqueness in strains associated with the non-hardening case. This discrepancy has also been observed in Mode I plane strain by LEVY *et al.* (1971) and RICE and TRACEY (1973). In this connection, it should also be mentioned that KNOWLES (1977), in working on the finite anti-plane shear field near a crack tip in an incompressible elastic solid, with a similar power law behaviour has made an important observation. He found that the first- and second-order terms in the asymptotic expansion for the displacements tend to become of equal importance, as one approaches the equivalent of the "perfectly plastic" case in such solids. This raises the question of whether the limit as $n \to \infty$ of the most singular term in the asymptotic

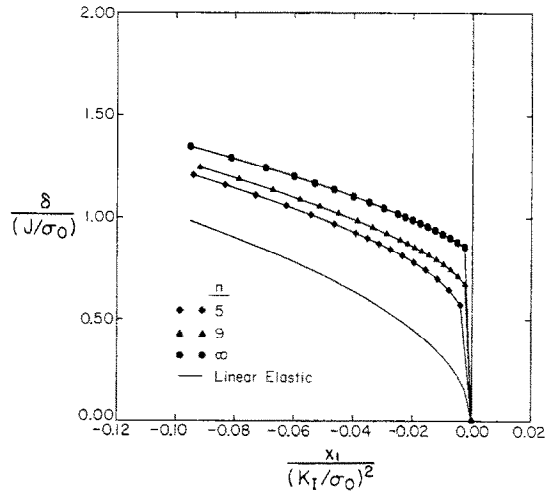

FIG. 10. Normalized crack opening profiles for several values of hardening.

solution can be considered separately, without examining the limiting behaviour of the higher-order terms of the expansion.

In order to resolve the issue further, a separate finite element calculation for the perfectly plastic case was performed under plane stress, small-scale yielding conditions using a focusing mesh with singular elements near the crack tip, similar to the work of RICE and TRACEY (1973). The results of this investigation will be reported in Section 6. Finally, it should be noted that the region ahead of the crack tip, wherein the $1/r$ variation of the plastic strains was observed ($r < 0.04(K_I/\sigma_0)^2$), corresponds to the region of dominance of the asymptotic stress field (see Fig. 6). Beyond this range, the front boundary of the fan may tend to curve and the $1/r$ variation for the plastic strains may no longer be valid (RICE, 1968a, b).

Crack opening displacement

The opening displacement between the crack faces as a function of position along the crack flank is shown in Fig. 10 in the nondimensional form, $\delta/(J/\sigma_0)$ versus $x_1/(K_I/\sigma_0)^2$, for the three cases, $n = 5$, 9 and ∞. The linear elastic solution corresponding to $n = 1$ is also plotted for comparison. J in this plot is the far-field value given by (3.3). From the figure, it can be observed that the amount of blunting at the crack tip increases with decreasing hardening (or increasing n). There is a discrete opening displacement at the tip for the perfectly plastic idealization because of reasons stated in Section 3.

On the other hand, the near-tip crack opening profile for the hardening cases, computed on the basis of the HRR analysis, has the form (HUTCHINSON, 1968a; RICE and ROSENGREN, 1968),

$$\delta = 2u_2(r, \pi) \sim (2r(\delta_t)^n)^{1/n+1}, \quad r \to 0. \tag{4.3}$$

In this expression, δ_t, which can be written as

$$\delta_t = \frac{J}{\sigma_0} \tilde{\delta}_t(\varepsilon_0, n), \tag{4.4}$$

can be approximately interpreted as the opening distance between the intercept of two 45° lines drawn back from the crack tip to the deformed profile. This definition was suggested by TRACEY (1976) as a measure of the crack tip displacement for a hardening material, since $\delta(r = 0) = 0$ in this case, as can be seen from (4.3). SHIH (1981) has obtained the values for $\tilde{\delta}_t(\varepsilon_0, n)$ from the HRR solution for both plane stress and plane strain. It is found (SHIH, 1981) that $\tilde{\delta}_t$ is strongly dependent on n and weakly on ε_0. Also, as $n \to \infty$, $\tilde{\delta}_t$ becomes independent of ε_0 and takes the value of 1.0 for plane stress.

From the present finite element calculation, the value of $\delta_t/(J/\sigma_0)$ was obtained by extrapolating the near-tip crack profile to $r = 0$ for the non-hardening case and by fitting the form (4.3) to the near-tip profile for the hardening cases. SHIH (1981) has also computed the values of $\delta_t/(J/\sigma_0)$ for several values of n from his finite element solution (SHIH, 1973), which as noted earlier employed a deformation plasticity theory. These results are summarized in the following table.

TABLE 1. *Values of* $\delta_t/(J/\sigma_0)$ *for plane stress*

	σ_0/E	$n = 5$	$n = 9$	$n = 25$	$n = \infty$
HRR	0.0012	0.40	0.63	0.89	1.0*
Present solution	0.0012	0.37	0.57		0.85
SHIH (1973, 1981)		0.38		0.86	

* (extrapolated).

The slightly smaller values for $\delta_t/(J/\sigma_0)$ obtained by the present solution, as compared to HRR for the hardening cases, can be accounted partially by some discrepancy between flow theory and deformation theory as explained below. But the difference between the present perfect plasticity calculation and the HRR non-hardening limit is because the latter is unable to provide complete information regarding the most singular term for the strains in the asymptotic solution for perfect plasticity, as described above. This discrepancy has also been observed in plane strain. The published numerical results (e.g., SHIH, 1981) for $\delta_t/(J/\sigma_0)$ under plane strain, small-scale yielding conditions for the perfectly plastic case range from 0.63 to 0.66, whereas the HRR non-hardening limit is 0.78.

J *integral calculations*

In order to assess the difference between the incremental formulation and the deformation plasticity theory, the path independence of the J integral was checked. The J integral (3.2) was computed for the hardening materials along several contours surrounding the crack tip, which passed through the centroids of the elements. The near-tip contours enclosing the crack tip were rectangular, while the far-field contours were circular, in keeping with the structure of the mesh (Fig. 1). The integrand in (3.2) was calculated, using the averaged values of stresses and strains at the centroids

of the elements lying in the contour path, and the integration was carried out numerically using Gauss quadrature. It was found that very near the crack tip ($r < 0.04r_p$) there was a small amount of path dependence. However, after some distance away from the crack tip, the calculated J value was virtually indistinguishable from the remotely applied value (3.3).

For a contour with an average radius $\bar{r} = 0.012(K_I/\sigma_0)^2$, the ratio of the calculated J value to the remotely applied J was 0.96 and 0.95 for $n = 5$ and 9, respectively. For contours with average radius $\bar{r} > 0.05(K_I/\sigma_0)^2$, the calculated J value was smaller than the applied J by less than 1%. While the 5% difference for the near-tip contours is within the realm of errors in the discretization procedure and in the numerical integration of (3.2), it also suggests small amounts of non-proportional loading experienced by a material particle from the time it was enveloped by the plastic zone. For the elastic–perfectly plastic material, our accurate numerical solution of Section 6 was used to estimate the near-tip J integral, and its discussion will be deferred till then.

In order to further check for discrepancy between the two plasticity theories, $\varepsilon_{22}^p/\varepsilon_0$ was calculated for the hardening materials at the centroids in the row of elements ahead of the crack tip by substituting the averaged stresses in these elements into the expression given by the J_2 deformation theory. The plastic strain given by the J_2 deformation theory was about 5% higher at $r = 0.012(K_I/\sigma_0)^2$ than the corresponding value given by the incremental formulation that was reported earlier (Fig. 8). This difference progressively diminished as the distance from the crack tip increased, and it was less than 1% for $r > 0.1(K_I/\sigma_0)^2$.

5. Numerical Simulation of Caustics

Introduction

The optical experimental method of caustics has been applied to the study of linear elastic fracture problems and to the direct measurement of the stress intensity factors (e.g., Theocaris and Gdoutos, 1972; Rosakis and Zehnder, 1985). This method was recently extended to the measurement of the J integral in ductile fracture (Rosakis *et al.*, 1983; Rosakis and Freund, 1982) on the basis of the validity of the plane stress, HRR asymptotic solution.

Under conditions of small-scale yielding, the singular elastic field dominates well outside the plastic zone. Inside the plastic zone, very near the crack tip, the HRR field dominates. In the transition region between these two fields, no analytical solution is available. This limits the applicability of caustics, and the conditions under which the results reported by Rosakis *et al.* (1983) and Rosakis and Freund (1982) are valid, are uncertain. Also, errors may be caused in the measurement of K_I based on the caustics obtained from the elastic region surrounding the plastic zone. This is because the crack tip plastic zone affects the caustic patterns, and an analysis based on the K_I field may be erroneous.

In this section, the full-field numerical solution under small-scale yielding is used to generate simulated caustic patterns. The numerical caustics are compared with the corresponding patterns observed from experiments (Zehnder *et al.*, 1986). The analysis of caustics based on the numerical results is not limited by the assumption

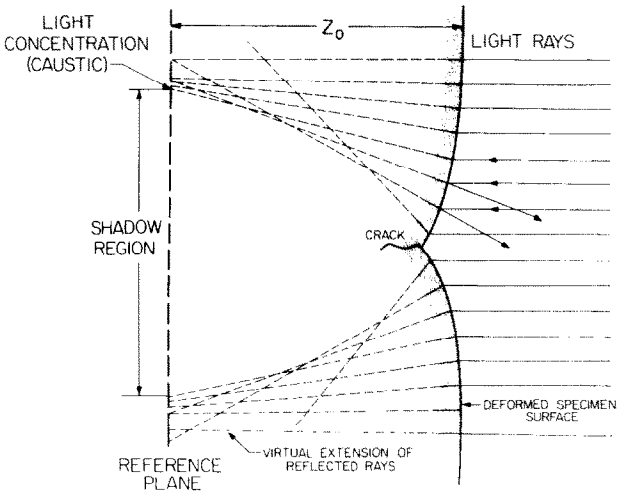

FIG. 11. Formation of caustic due to reflection of light from a polished, deformed specimen surface.

of the validity of any particular asymptotic field. Finally, qualitative and quantitative comparisons of the simulated caustics, obtained at various distances from the crack tip, are made with the corresponding results based on the near-tip HRR analysis and the remotely applied K_I field.

The method of caustics

Consider a set of parallel light rays normally incident on a planar, reflective specimen that has been deformed by tensile loading. Due to the deformed shape of the specimen, an envelope in space called the "caustic surface" is formed by the virtual extension of the reflected light rays (Fig. 11). The intersection of this surface with a plane located at a distance z_0 behind the specimen is called the "caustic curve" and it bounds a dark region called the "shadow spot".

Let (x_1, x_2) be a coordinate system on the specimen surface centered at the crack tip and (X_1, X_2), a system translated by a distance z_0 behind the specimen surface. Then the mapping of a point (x_1, x_2) on the specimen surface to a point (X_1, X_2) on the plane at z_0 due to reflection of a light ray may be described by (ROSAKIS and ZEHNDER, 1985)

$$X_\alpha = x_\alpha + 2z_0 \frac{\partial u_3(x_1, x_2)}{\partial x_\alpha}. \tag{5.1}$$

The locus of points on the specimen surface at which the Jacobian determinant of the mapping (5.1) vanishes is called the "initial curve". While points on the initial curve map onto the caustic curve, all points both inside and outside the initial curve map outside the caustic. The position of the initial curve may be varied by changing z_0.

For a stationary crack under small-scale yielding conditions, if the initial curve is chosen to fall well outside the plastic zone and within the region of validity of the K_I field (large values of z_0), then the resulting caustic curve will be an epicycloid (Fig. 12(a)). In such a case, K_I is related to the caustic diameter D (which is the maximum

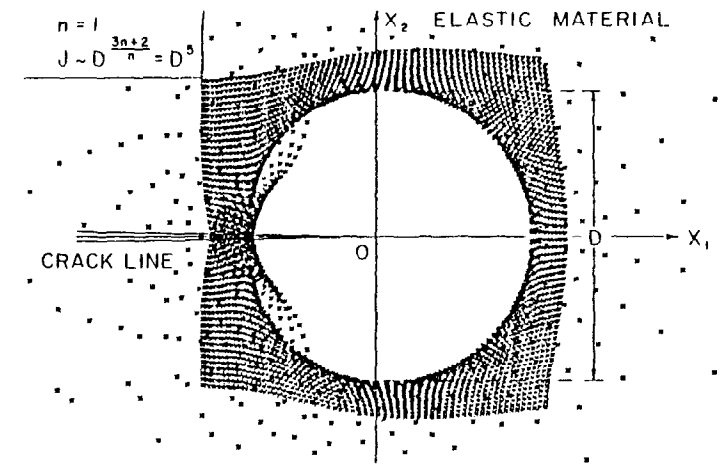

(a)

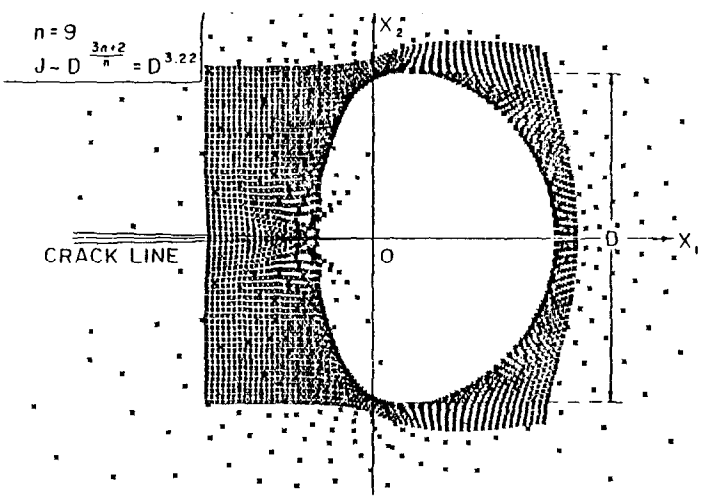

(b)

FIG. 12. Predicted caustic shapes based on (a) K_I field and (b) HRR asymptotic field for $n = 9$.

width of the caustic in the X_2 direction) by (ROSAKIS and ZEHNDER, 1985),

$$K_I = \frac{ED^{5/2}}{10.7z_0\sqrt{vh}}, \tag{5.2}$$

where h is the specimen thickness. The initial curve is circular and its radius r_0 is given by

$$r_0 = 0.316\,D. \tag{5.3}$$

On the other hand, if the initial curve is chosen to fall well inside the plastic zone and within the region of dominance of the HRR field (very small values of z_0), then its shape as deduced by ROSAKIS *et al.* (1983) will no longer be circular. In such a case, the radius r_0 of the point on the initial curve that maps to the maximum value of X_2 on the caustic curve is given by

$$r_0 = 0.385\,D, \tag{5.4}$$

for a hardening exponent n of 9. Also, the value of the J integral may be obtained from the caustic diameter D as (ROSAKIS *et al.*, 1983),

$$J = S_n \frac{\sigma_0^2}{E}\left[\frac{E}{\sigma_0 z_0 h}\right]^{(n+1)/n} D^{(3n+2)/n}, \tag{5.5}$$

where S_n is a numerical factor dependent on n. Caustic curves thus obtained from the HRR field for several values of the hardening exponent are given by ROSAKIS *et al.* (1983). A typical caustic for $n = 9$ is shown in Fig. 12(b).

Results and discussion

The discrete values of the out-of-plane displacement u_3 obtained from the numerical solution at the centroids of the elements were smoothed using a least-squares finite element scheme as advocated by HINTON and CAMPBELL (1974). The surface thus generated is shown in Fig. 13 for a material with a hardening exponent of 9. Caustic patterns were simulated by mapping light rays point by point from this smoothed surface using (5.1) for different values of z_0.

The sequence of caustics simulated from the finite element solution for different values of z_0 is shown in Fig. 14 for a material with $n = 9$. The parameter r_0/r_p in the figure is the ratio of the initial curve size to the maximum plastic zone extent. The initial curve size r_0 was estimated approximately by using (5.4) for caustics from within the plastic zone and by (5.3) for caustics from outside the plastic zone. It is seen from the figure that for $r_0/r_p = 0.19$, the simulated caustic agrees in shape with the caustic predicted by the HRR field, which is shown in Fig. 12(b). When $r_0/r_p = 1.3$, the numerically simulated caustic, Fig. 14(f), agrees with the caustic predicted using the elastic, K_I field (Fig. 12(a)).

A sequence of photographs of caustics (ZEHNDER *et al.*, 1986) obtained from the tensile loading of a thin compact tension specimen of 4340 carbon steel is shown in Fig. 15. The experimental details, specimen dimensions, etc. are described by ZEHNDER *et al.* (1986). On comparing Figs 14 and 15 it is seen that in both cases there is a

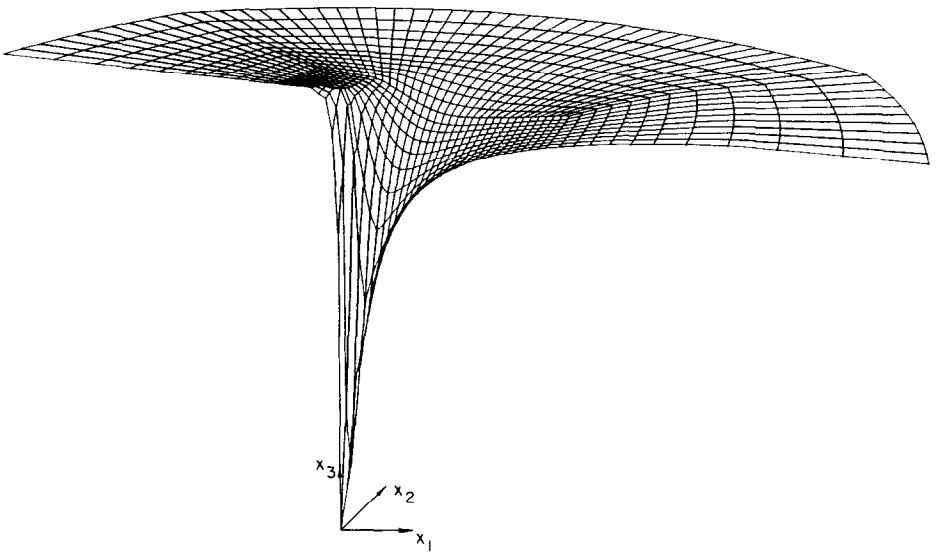

FIG. 13. Smoothed out-of-plane displacement field for $n = 9$.

transition from an "HRR caustic" to an "elastic caustic" as r_0/r_p goes from 0.19 to 1.4. The transition away from the HRR caustic appears to take place slightly sooner in the numerical model (around $r_0/r_p = 0.3$) than in the experiment (around $r_0/r_p = 0.35$). However, the general trend is similar in both cases.

It is found that both the numerical and experimental caustics retain the shape predicted by the K_I field even for r_0/r_p as small as 1.0. Thus, the effect of the plastic zone cannot be judged by mere observation of the caustic shape. The reason for the invariance in shape of the caustics is explained by examining the angular variation of the sum $(\sigma_{11}+\sigma_{22})$, of the direct stress components (as given by the numerical solution), at different distances outside the plastic zone as shown in Fig. 16. It is seen that the sum $(\sigma_{11}+\sigma_{22})$ generally follows the angular distribution given by the K_I field, which is shown by the solid line in the figure even for r_0/r_p as small as 1.2. However, the individual stress components show more deviation from those of the K_I field for small values of r_0/r_p. This observation is important, since the caustic shape depends on the angular variation of the out-of-plane displacement component u_3, which in the elastic region, is proportional to $(\sigma_{11}+\sigma_{22})$ under plane stress. Thus, it is not surprising that the caustic shape resembles the "elastic caustic" for r_0/r_p as small as 1.0.

The numerical caustics were simulated for a fixed value of K_I (or the far-field value of J as given by (3.3)) by varying z_0 in the optical mapping (5.1). The relationship between the diameter D of the simulated caustics and the remotely applied J value is shown in non-dimensional form in Fig. 17. The inverse of the abscissa in the figure is an indication of the initial curve size or the distance from the crack tip at which the information about the deformation field is being scrutinized. Thus a very small abscissa value (large z_0 or small J) implies that the initial curve is far away from the tip. A very large abscissa value, on the other hand, implies that the curve is very near

the tip, probably within the range of dominance of the HRR field. The bars on the numerical results indicate the uncertainty in determining the initial curve due to discretization of the finite elements.

The solid line in the figure represents the variation of caustic size in the K_I dominated region as given by (5.2) with $\nu = 0.3$. The dashed line gives the relationship for the caustics from the HRR-dominated region (5.5). As can be observed from this figure, the numerical results approach the elastic relation (5.2) for small abscissa values and the relation (5.5) obtained from the HRR solution for large values of the abscissa. In the intermediate region there is a transition from one distribution to the other.

6. SINGULAR FINITE ELEMENT ANALYSIS

Introduction

In this section, a detailed investigation of the perfectly plastic case will be presented, with the view of examining closely the discrepancy between the numerical results for the near-tip strains and the corresponding term of the HRR solution (non-hardening limit), which was noted in Section 4. For this purpose, a singular finite element analysis similar to the plane strain work of RICE and TRACEY (1973) was carried out under Mode I plane stress, small-scale yielding conditions. A ring of focused isosceles triangular-shaped elements was used near the crack tip in this computation. This mesh design is different from the fine mesh employed in the earlier analysis (Fig. 1(b)). Thus, the issue of sensitivity of the numerical results presented earlier in Section 4 to the near-tip mesh design was also examined through this section of our work.

Numerical scheme

The near-tip elements that were employed here provide a capability for non-uniqueness of displacement at the crack tip (LEVY *et al.*, 1971; RICE and TRACEY, 1973), which is the fundamental feature of the $1/r$ plastic strain singularity within centred fan regions (Section 3). This was achieved by treating the triangular elements at the crack tip as degenerate isosceles trapezoids that have a total of four nodes (one at each vertex) with two nodes coinciding at the crack tip (Fig. 18). The coincident nodes at the crack tip were constrained to move as a single point till the load level at which incipient yielding was detected in one of the near-tip elements. A special shape function (RICE and TRACEY, 1973) was used up to this load level to provide the crack tip elements the capability to model the $1/\sqrt{r}$ dominant elastic strain singularity. Subsequently, the coincident nodes were allowed to move independently and the crack tip elements modelled the $1/r$ plastic strain singularity.

The mapping of a four-noded rectangle to a triangle (Fig. 18) can be described by

$$\mathbf{x} = \mathbf{x}^i \frac{(1-\xi)(1+\eta)}{4} + \mathbf{x}^j \frac{(1-\xi)(1-\eta)}{4} + \mathbf{x}^k \frac{(1+\xi)(1-\eta)}{4} + \mathbf{x}^l \frac{(1+\xi)(1+\eta)}{4}, \tag{6.1}$$

with the constraint $\mathbf{x}^j = \mathbf{x}^l$. Here (ξ, η) is the natural coordinate system for the element

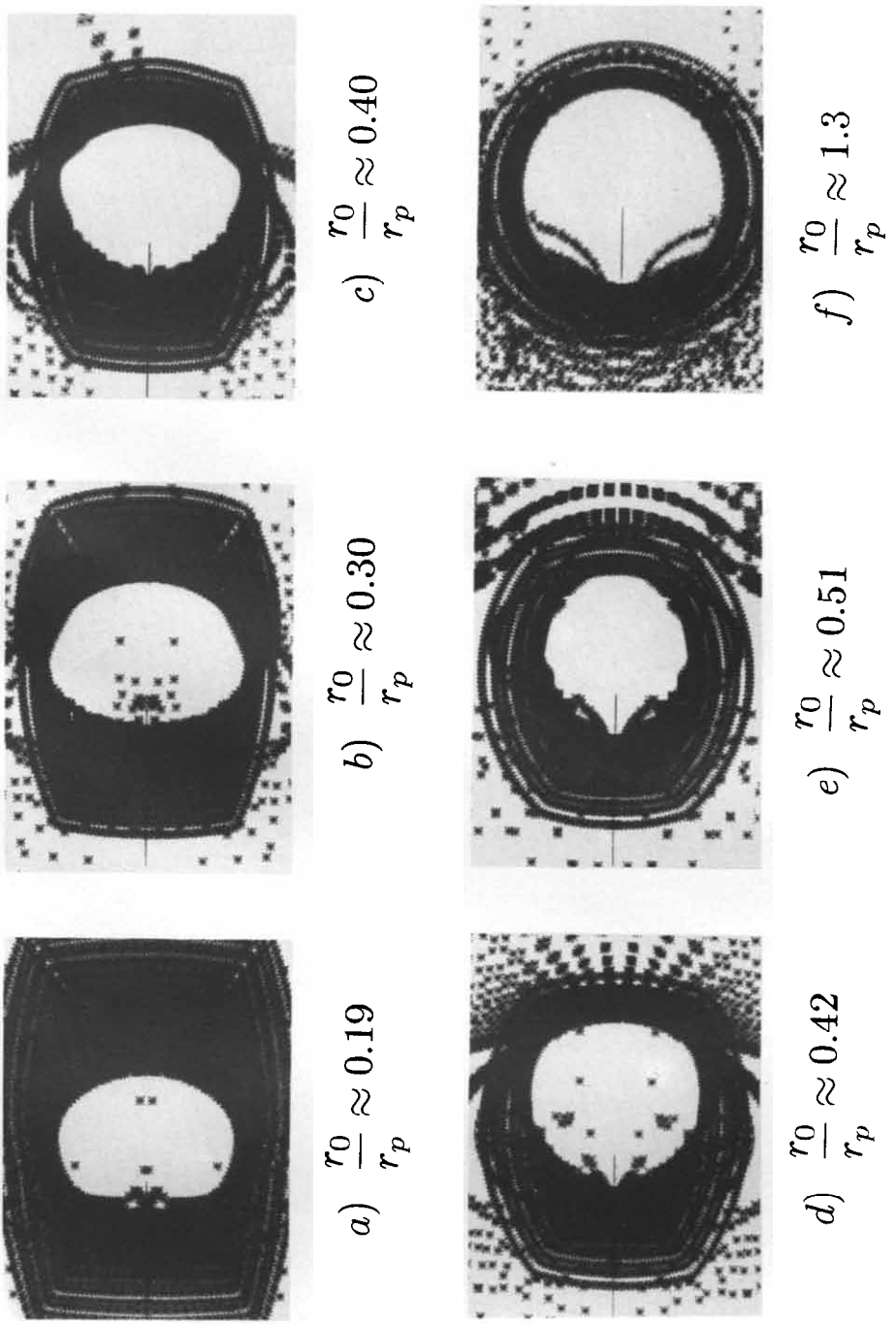

FIG. 14. Sequence of caustics simulated from the numerical solution.

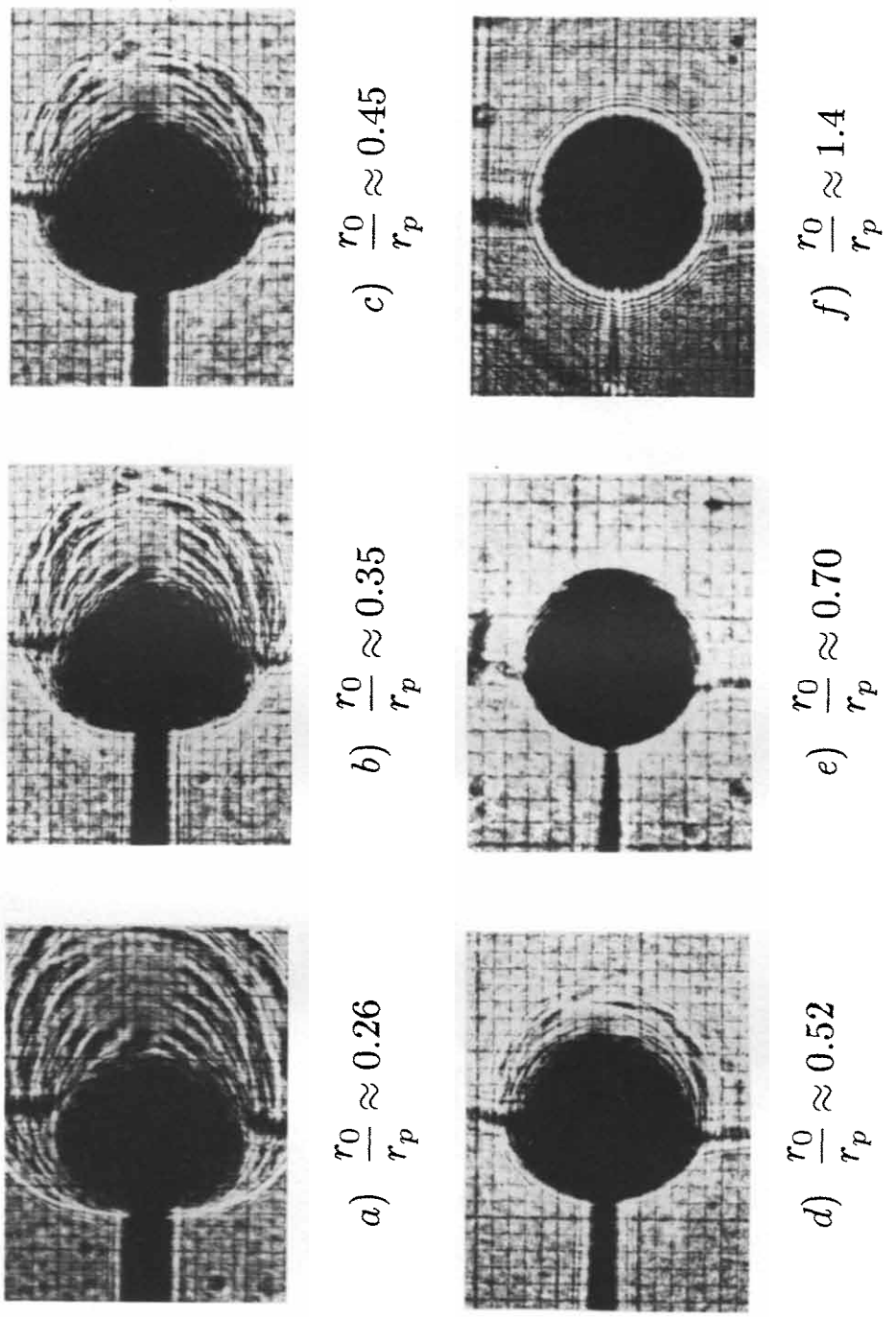

FIG. 15. Sequence of caustics obtained from experiments (ZEHNDER *et al.*, 1986).

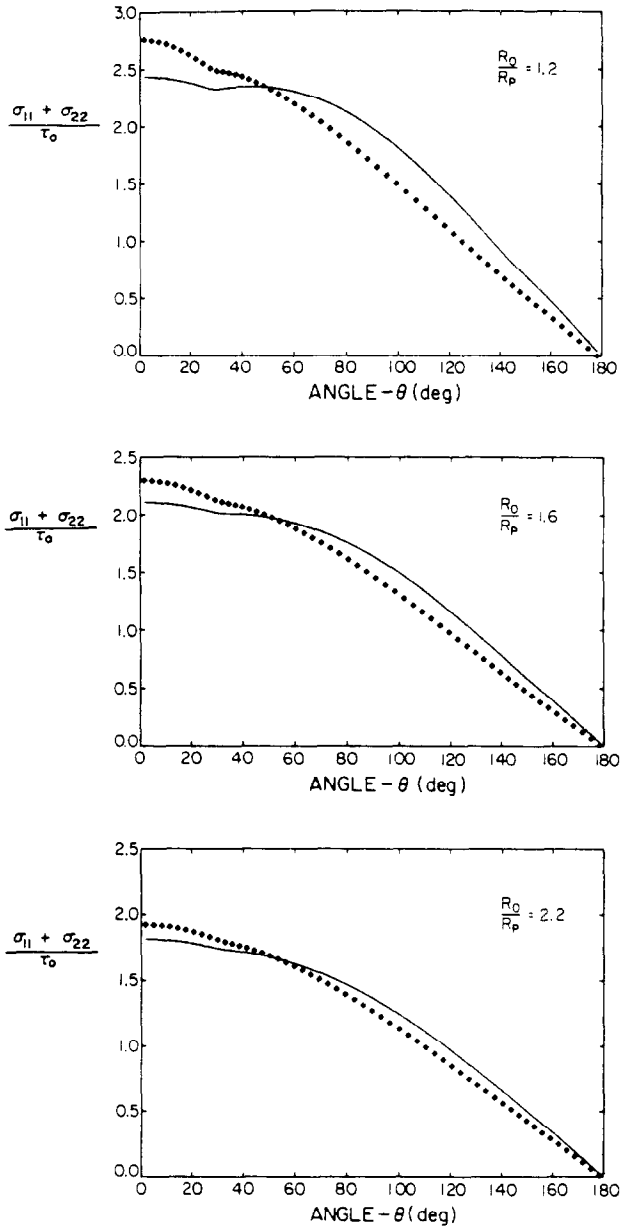

FIG. 16. Angular distribution of $(\sigma_{11}+\sigma_{22})$ for different distances from the tip. The solid line is the distribution given by the K_I field.

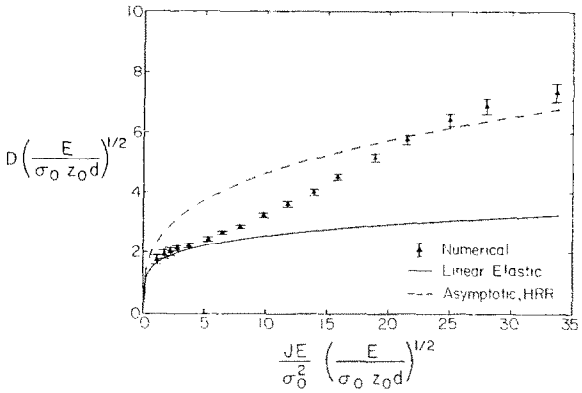

FIG. 17. Relationship between caustic diameter and the J integral as obtained from the numerically simulated caustics.

and (x_1, x_2) is a global coordinate system centered at the crack tip. The inverse mapping of (ξ, η) in terms of a local Cartesian coordinate system (s, t), and a local polar coordinate system (r, ψ) for the element is given by (Fig. 18),

$$\left.\begin{aligned} \xi &= \frac{2s}{s_0} - 1 \\ \eta &= \frac{t/s}{(t_0/s_0)} = \frac{\tan\psi}{\tan\alpha} \end{aligned}\right\}. \tag{6.2}$$

The elastic singularity element has the shape function (RICE and TRACEY, 1973),

$$\mathbf{u} = \mathbf{u}^{ij}\left(1 - \sqrt{\frac{1+\xi}{2}}\right) + \mathbf{u}^{k}\frac{(1-\eta)}{2}\sqrt{\frac{1+\xi}{2}} + \mathbf{u}^{l}\frac{(1+\eta)}{2}\sqrt{\frac{1+\xi}{2}}. \tag{6.3}$$

Here $\mathbf{u}^{ij}$ represents the unique displacement of the crack tip nodes i and j. The above element correctly models the $\sqrt{r}$ variation in the leading term for the displacements of the linear elastic solution. Also, displacement compatibility is satisfied along the edges i–l and j–k ($\eta = \pm 1$) with the adjacent singular elements and along the edge l–k ($\xi = 1$) with the conventional four-noded isoparametric element that is joined there.

As was first pointed out by LEVY *et al.* (1971), the mapping of any four-noded isoparametric element to a triangle leads to a $1/r$ strain variation provided that the coincident nodes are permitted to have different displacements. The crack tip displacement for such an element is given by (Fig. 18),

$$\mathbf{u}(-1, \eta) = \frac{(\mathbf{u}^{i} + \mathbf{u}^{j})}{2} + \eta\frac{(\mathbf{u}^{i} - \mathbf{u}^{j})}{2}. \tag{6.4}$$

Following the notation of (3.9) and neglecting the elastic strains that are bounded, it can be shown from (6.4) that

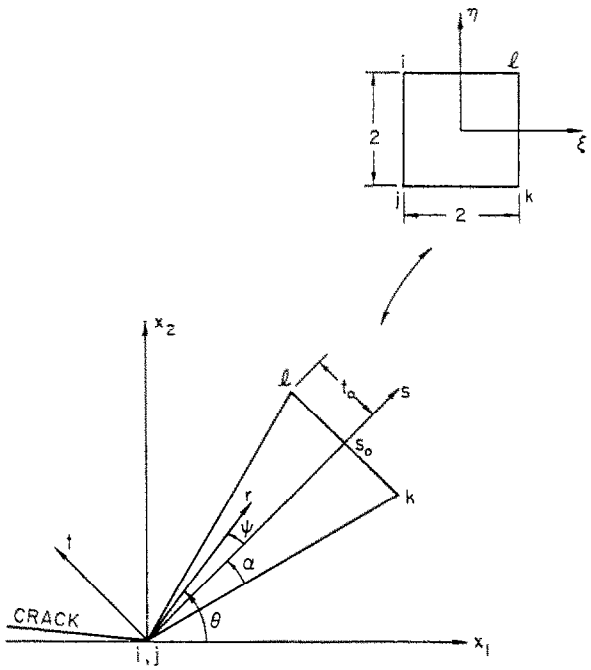

FIG. 18. Typical near-tip element used in the singular finite element analysis.

$$\left.\begin{aligned}\hat{\varepsilon}^p_{\theta\theta} &= \frac{E}{\sigma_0}\left(\frac{\sec\psi}{2\tan\alpha}\right)[-(u_s^i-u_s^j)\tan\psi+(u_t^i-u_t^j)]\\ \hat{\varepsilon}^p_{r\theta} &= \frac{E}{\sigma_0}\left(\frac{\sec\psi}{4\tan\alpha}\right)[(u_s^i-u_s^j)+(u_t^i-u_t^j)\tan\psi]\end{aligned}\right\}, \tag{6.5}$$

where u_s and u_t are the displacement components in the local (s, t) Cartesian coordinate system and ψ is the angle measured in the local (r, ψ) polar coordinate system (Fig. 18) for the element. It should be noted that the right-hand side of (6.5) is a first-order finite difference approximation to $\hat{\varepsilon}^p_{\theta\theta}(\psi)$ and $\hat{\varepsilon}^p_{r\theta}(\psi)$. Also, it should be noted that if the two coincident nodes displace as a single point, so that $\mathbf{u}^i = \mathbf{u}^j$, then this element behaves as an ordinary constant strain triangle.

The mesh employed in this analysis was similar to the one used by LEVY *et al.* (1971). Only the upper half-plane was considered because of symmetry. The active mesh consisted of 20 rings with radii of L, $(1.5)^2\,L$, $(2.0)^2\,L$, ..., $(9.5)^2\,L$, $(10.0)^2\,L$ and 115 L. These were divided by 25 rays at equal angular intervals of 7.5°, giving a total of 525 nodes (including 25 coincident crack tip nodes) and 480 elements in the active mesh. The region outside consisted of 14 rings with 24 elements in each ring and always remained elastic. Static condensation was employed in this region as described in Section 2. The radius of the outermost boundary S on which the displacement boundary condition (2.1) was specified was 645 L. The loading process was stopped when the maximum plastic zone extent was about $\frac{1}{15}$ of the radius of the outermost boundary S, so that the small-scale yielding condition was preserved. The

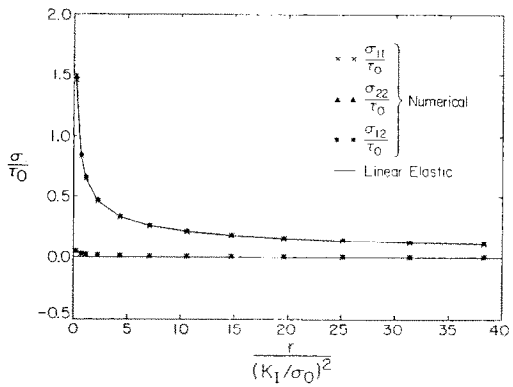

FIG. 19. Radial distribution of stresses ahead of crack tip at incipient yielding. Solid line is the singular elastic solution.

symmetry condition (2.2) on the $\theta = 0$ ray and the traction-free condition on the $\theta = \pi$ ray were enforced.

Every near-tip element was composed of three subelements (RICE and TRACEY, 1973), each extending to one-third of the height of the element. A nine-point numerical integration scheme was employed to integrate the element stiffness matrix, with integration stations at $(\xi, \eta = -\frac{3}{5}, 0, \frac{3}{5})$ and weighting factors of $\frac{1}{9}$ of the area of the element. For the isoparametric elements outside the innermost ring, the two-by-two Gauss quadrature scheme was used. The solution strategy was the same as that described in Section 2 with the additional modifications mentioned earlier in this section.

Results and discussion

It can be shown by substituting the dominant term of the elastic solution for the stresses into the plane stress Von Mises yield condition that incipient yielding will occur at an angle of $\arccos(\frac{1}{3}) \approx 70.5°$. Also, the value of the load parameter, $K_I^c/(\sigma_0\sqrt{2\pi r_y})$, calculated from the analytical solution is 0.866 for initial yielding at a radius of r_y. Incipient yielding occurred in the present finite element computation in the subelement between 67.5° and 75° with a mean angle of 71.25°. The value of $K_I^c/(\sigma_0\sqrt{2\pi r_y})$ was 0.83, which is in good agreement with the analytical prediction.

The radial distribution of stresses along the ray ahead of the crack tip at incipient yield is shown in Fig. 19 in the nondimensional form, σ/τ_0 versus $r/(K_I/\sigma_0)^2$. The stresses given by the finite element solution are in excellent agreement with the dominant elastic solution, which is shown by the solid line in the figure. Also, the angular distribution of stresses within the crack tip elements compared closely with the analytical solution.

The plastic zone at the end of the stationary load history is shown in nondimensional coordinates in Fig. 20. This compares very well, in overall features, with the plastic zone obtained in the earlier analysis (Fig. 3). The maximum plastic zone extent is

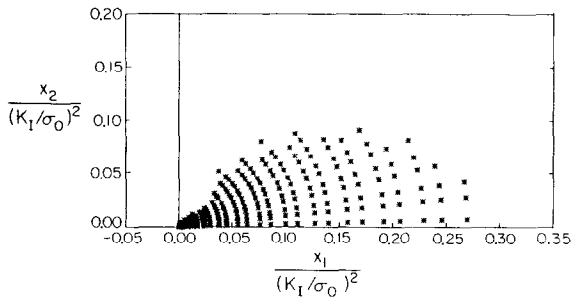

FIG. 20. Plastic zone for the perfectly plastic case obtained from the singular finite element analysis.

about $r_p = 0.28(K_I/\sigma_0)^2$ ahead of the crack tip. In the subelements nearest to the crack tip, yielding spread only from $\theta = 0$ to 75°, which is in approximate agreement with the centered fan region of Fig. 2.

The radial stress distribution ahead of the crack tip within the plastic zone also appeared similar to the variation reported earlier in Fig. 6. In the subelement nearest to the crack tip that occupies the angular range from $\theta = 0$ to 7.5°, the stresses σ_{11} and σ_{22} reached the constant values 0.99 τ_0 and 1.999 τ_0, respectively, which agrees very well with the analytical asymptotic limit (3.7). Once again, a strong radial variation in the σ_{11} stress component was observed along the $\theta = 0$ ray, with a value at the elastic–plastic boundary of 1.40 τ_0.

The angular distribution of the normalized stress component $\sigma_{\theta\theta}/\tau_0$, within the subelements nearest to the tip, is shown in Fig. 21 along with the slip line solution (solid line) of HUTCHINSON (1968b). The finite element solution shows good agreement with the analytical distribution in the angular range $0 < \theta < 80°$, which corresponds to the centered fan region in Fig. 2. This was typical of the other two stress components $\sigma_{r\theta}$ and σ_{rr} as well, with σ_{rr} showing more deviation from the analytical solution as $\theta \to 80°$. This result is consistent with the fact that the two constant stress sectors in Fig. 2 were not detected by the finite element solution. Also, the numerical result suggests that within the fan, the focusing of the slip lines may occur very close to the crack tip in the angular range $65° < \theta < 80°$.

The normalized crack tip opening displacement $\delta_t/(J/\sigma_0)$, where J is the remotely applied value of the J integral, was calculated based on the crack tip node lying on the $\theta = \pi$ ray. It increased from zero at incipient yield ($K_I = K_I^\circ$) to a constant value of 0.84 at $K_I \approx 3.5\ K_I^\circ$. This value did not change during the subsequent part of the loading process. The variation in $\delta_t/(J/\sigma_0)$ during the initial phase of the loading process occurred since the plastic zone was not fully developed. It should be noted that this quantity is in excellent agreement with the value reported in Table 1, which was calculated on the basis of the earlier analysis.

The displacements of the crack tip nodes were substituted into equation (6.5), with $\psi = 0$ (corresponding to the mean angle of the near-tip element), to determine the angular factors $\hat{\varepsilon}^p_{\theta\theta}(\theta)$ and $\hat{\varepsilon}^p_{r\theta}(\theta)$ of the dominant $1/r$ strain singularity (3.9). In order to compare with the dimensionless angular factors $\tilde{\varepsilon}^p_{ij}(\theta, n)$ given by the HRR analysis (equation (3.1)) for large n, the functions $\hat{\varepsilon}^p_{\theta\theta}(\theta)$ and $\hat{\varepsilon}^p_{r\theta}(\theta)$ obtained from the present finite element calculation for the perfectly plastic case were normalized as follows,

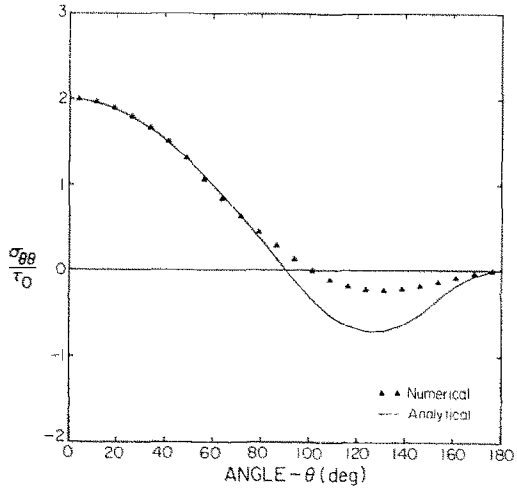

FIG. 21. Angular distribution of $\sigma_{\theta\theta}/\tau_0$ within sub-elements closest to the crack tip at the end of the loading process. Solid line is the analytical, asymptotic solution of HUTCHINSON (1968b).

$$\left.\begin{aligned} \tilde{\varepsilon}^p_{\theta\theta}(\theta) &= \frac{\hat{\varepsilon}^p_{\theta\theta}(\theta)}{(K_1/\sigma_0)^2} I_n \\ \tilde{\varepsilon}^p_{r\theta}(\theta) &= \frac{\hat{\varepsilon}^p_{r\theta}(\theta)}{(K_1/\sigma_0)^2} I_n \end{aligned}\right\}. \tag{6.6}$$

Here I_n is taken as 2.6 corresponding to $n \to \infty$ in the HRR solution. The functions thus obtained are shown along with the HRR distribution for $n = 25$ (which is given by SHIH (1973)) in Fig. 22. It can be seen that the two angular functions are completely different. It is interesting to note that the numerical solution for the perfectly plastic case under small-scale yielding conditions gives vanishingly small values for the angular factors of the dominant $1/r$ strain singularity for $\theta > 45°$, although the slip line solution of Fig. 2 shows a centered fan extending from $\theta = 0$ to about 80°.

It is found that the angular factors $\hat{\varepsilon}^p_{\theta\theta}$ and $\hat{\varepsilon}^p_{r\theta}$, obtained from the numerical solution, satisfy almost exactly the following relation,

$$\hat{\varepsilon}^p_{r\theta}(\theta) = \hat{\varepsilon}^p_{\theta\theta}(\theta) \frac{\sin\theta}{\cos\theta}, \tag{6.7}$$

which is analogous to equation (3.11), as applied to the accumulated near-tip plastic strains. Also, as was observed from the near-tip strain distribution (Fig. 9) of the earlier analysis, it is again found from the present computation (Fig. 22) that $\tilde{\varepsilon}^p_{\theta\theta}(\theta = 0)$ for the perfectly plastic case is about 3.3 times the corresponding value given by the HRR analysis for large n.

The near-tip value of the J integral was calculated by substituting $\hat{\varepsilon}^p_{\theta\theta}(\theta)$ and $\hat{\varepsilon}^p_{r\theta}(\theta)$ obtained above into equation (3.15). The integral in (3.15) was estimated numerically, and it was found that J_{tip} is about 0.95 times the remotely applied J

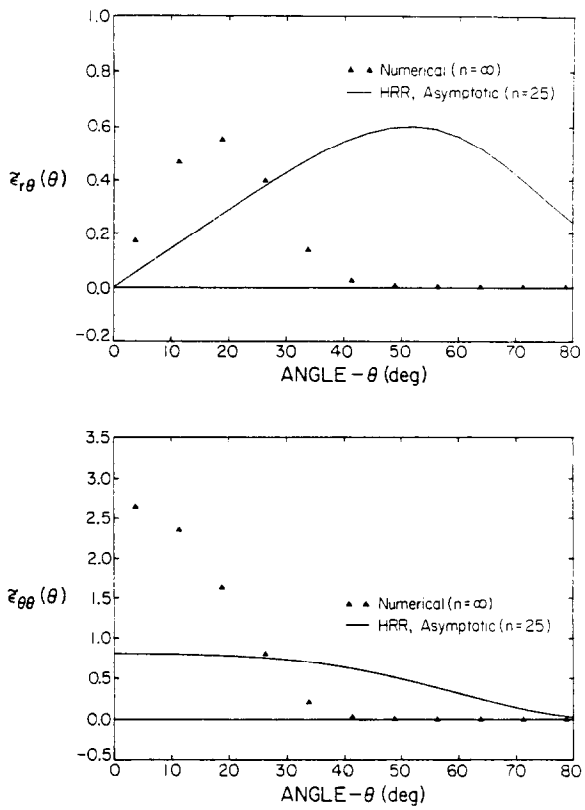

FIG. 22. The angular factors of the $1/r$ plastic strain singularity obtained from the numerical solution on the basis of the non-unique crack tip displacement. Solid line is the variation given by the HRR solution for $n = 25$ (SHIH, 1973).

value. This is somewhat different from the development in plane strain where TRACEY (1976) reported J_{tip} to be about 0.8 times the applied J value. But later, SHIH (1981) found J_{tip} to be 0.96 times the applied J from his finite element calculation under plane strain, small-scale yielding conditions for the perfectly plastic case based on a different type of singular element.

If the near-tip J computed above from the present analysis is used to normalize the crack tip displacement δ_t, it is found that $\delta_t = 0.88(J_{tip}/\sigma_0)$. Hence, it is concluded that $\delta_t/(J/\sigma_0)$ for the perfectly plastic case under plane stress, small-scale yielding conditions could vary from 0.84 to 0.88.

In closing, it is observed that all the results given above by the present accurate numerical computation are in good agreement, in every respect, with the earlier analysis, which employed a nonfocusing mesh with nonsingular elements near the crack tip. The earlier analysis relied purely on the fineness of the mesh and a large plastic zone to the smallest element size ratio to provide sufficient resolution near the crack tip.

ACKNOWLEDGEMENTS

The authors would like to express their gratitude to Professors J. K. KNOWLES and J. F. HALL for their valuable advice and encouragement. This investigation was supported by the Office of Naval Research through ONR contract # N0014-85-K-0596. The computations were performed using the Supercomputer at Boeing Computer Services, Seattle. This was made possible through NSF contract # MEA-8307785. The above contracts and the facilities provided by Boeing Computer Services are gratefully acknowledged.

REFERENCES

BATHE, K. J. 1982 *Finite Element Procedures in Engineering Analysis.* Prentice Hall, Englewood Cliffs, New Jersey.

BATHE, K. J. and CIMENTO, A. P. 1980 *Comp. Meth. appl. mech. Engr.* **22,** 59.

BEGLEY, J. A. and LANDES, J. D. 1972 *Fracture Toughness*, ASTM STP 514, p. 1. American Society for Testing and Materials, Philadelphia.

HILL, R. 1983 *The Mathematical Theory of Plasticity*. Clarendon Press, Oxford, paperback.

HILTON, P. D. and HUTCHINSON, J. W. 1971 *Engng Frac. Mech.* **3,** 435.

HINTON, E. and CAMPBELL, J. S. 1974 *Int. J. num. Meth. Engng* **8,** 461.

HUTCHINSON, J. W. 1968a *J. Mech. Phys. Solids* **16,** 13.

HUTCHINSON, J. W. 1968b *J. Mech. Phys. Solids* **16,** 337.

KNOWLES, J. K. 1977 *Int. J. Fracture* **13,** 611.

LANDES, J. D. and BEGLEY, J. A. 1972 *Fracture Toughness*, ASTM STP 514, p. 24. American Society for Testing and Materials, Philadelphia.

LEVY, N., MARCAL, P. V., RICE, J. R. and OSTERGREN, W. J. 1971 *Int. J. Fracture Mech.* **7,** 143.

MCMEEKING, R. M. 1977 *J. Mech. Phys. Solids* **25,** 357.

MCMEEKING, R. M. and PARKS, D. M. 1979 *Elastic Plastic Fracture*, ASTM STP 668, p. 175. American Society for Testing and Materials, Philadelphia.

NAGTEGAAL, J. C., PARKS, D. M. and RICE, J. R. 1974 *Comp. Meth. appl. mech. Engr.* **4,** 153.

RICE, J. R. 1968a *J. appl. Mech.* **35,** 379.

RICE, J. R. 1968b *Fracture: An Advanced Treatise* (edited by H. LIEBOWITZ), Vol. 2, p. 191. Academic Press, New York.

RICE, J. R. and ROSENGREN, G. F. 1968 *J. Mech. Phys. Solids* **16,** 1.

RICE, J. R. and TRACEY, D. M. 1973 *Numerical and Computer Methods in Structural Mechanics* (edited by S. J. FENVES *et al.*), p. 585. Academic Press, New York.

ROSAKIS, A. J. and FREUND, L. B. 1982 *Trans. ASME, J. Engrs Mat. and Tech.* **104,** 115.

ROSAKIS, A. J., MA, C. C. and FREUND, L. B. 1983 *J. appl. Mech.* **50,** 777.

ROSAKIS, A. J. and ZEHNDER, A. T. 1985 *J. Elasticity* **15,** 347.

SCHREYER, H. L., KULAK, R. F. and KRAMER, J. M. 1979 *Trans. ASME, J. Press. Ves. Tech.* **101,** 226.

SHIH, C. F. 1973 *Elastic–Plastic Analysis of Combined Mode Fracture Problems.* Ph.D. dissertation, Harvard University, Cambridge, MA.

SHIH, C. F. 1981 *J. Mech. Phys. Solids* **29,** 305.

SHIH, C. F. and GERMAN, M. D. 1981 *Int. J. Fracture* **17,** 27.

TADA, H., PARIS, P. and IRWIN, G. 1973 *The Stress Analysis of Cracks Handbook.* Del Research Corporation, Hellertown.

THEOCARIS, P. S. and GDOUTOS, E. E. 1972 *J. Appl. Mech.* **39,** 91.

TRACEY, D. M. 1976 *Trans. ASME, J. Engrs Mat. and Tech.* **98,** 146.

ZEHNDER, A. T., ROSAKIS, A. J. and NARASIMHAN, R. 1986 *Measurement of J Integral with Caustics: An Experimental and Numerical Investigation.* Caltech Report SM 86-8, Pasadena, CA.

APPENDIX

Newton-Raphson method for equilibrium iteration

It was observed in Section 2 that an iterative Newton-Raphson method was used in the solution of the incremental equilibrium equations (2.11). This procedure is summarized below for the kth equilibrium iteration of the $(t+\Delta t)$th time step.

(1) The externally applied load is increased and $\mathbf{F}(t+\Delta t)$ is calculated.

(2) The tangent stiffness matrix $\mathbf{K}_T^{k-1}(t+\Delta t)$ and the vector $\mathbf{P}^{k-1}(t+\Delta t) = \int_R \mathbf{B}^T \boldsymbol{\sigma}^{k-1}(t+\Delta t)\,\mathrm{d}A$ are calculated. For the first iteration of the time step ($k = 1$), the above vector is computed from the converged solution at the end of the previous time step as $\mathbf{P}^0(t+\Delta t) = \int_R \mathbf{B}^T \boldsymbol{\sigma}(t)\,\mathrm{d}A$.

(3) The following matrix equation is solved by Gauss elimination:

$$\mathbf{K}_T^{k-1}\Delta\mathbf{U}^k = \mathbf{F}(t+\Delta t) - \mathbf{P}^{k-1} = \Delta\mathbf{R}^k.$$

(4) The nodal displacements and element strains are updated as follows,

$$\mathbf{U}^k(t+\Delta t) = \mathbf{U}^{k-1}(t+\Delta t) + \Delta\mathbf{U}^k$$

$$\boldsymbol{\varepsilon}^k(t+\Delta t) = \mathbf{B}\mathbf{U}^k(t+\Delta t).$$

For the first iteration of the time step ($k = 1$),

$$\mathbf{U}^1(t+\Delta t) = \mathbf{U}(t) + \Delta\mathbf{U}^1.$$

(5) In order to prevent fictitious (numerical) elastic unloading of elements in some parts of the plastic zone during the subsequent iterations ($k > 1$) of the time step, a path independent scheme is used to update element stresses. The stresses are estimated by integrating from the values at the end of the previous accepted equilibrium configuration to the current iteration of this time step by using the cumulative strains as follows (BATHE, 1982),

$$\boldsymbol{\sigma}^k(t+\Delta t) = \boldsymbol{\sigma}(t) + \int_{\boldsymbol{\varepsilon}(t)}^{\boldsymbol{\varepsilon}^k(t+\Delta t)} \mathbf{D}\,\mathrm{d}\boldsymbol{\varepsilon}$$

An explicit method was employed to evaluate the integral in the above equation.

(6) The Euclidean norm of the out-of-balance force vector $\Delta\mathbf{R}^k$ (see Step (3)) and the internal energy increment are checked for convergence by comparing with the corresponding values at the start of the iteration process as (BATHE and CIMENTO, 1980),

$$\|\Delta\mathbf{R}^k\| \leqslant \delta_F \|\Delta\mathbf{R}^1\|,$$

$$\Delta\mathbf{U}^k \cdot \Delta\mathbf{R}^k \leqslant \delta_E \Delta\mathbf{U}^1 \cdot \Delta\mathbf{R}^1,$$

where δ_F and δ_E are small, preset tolerances.

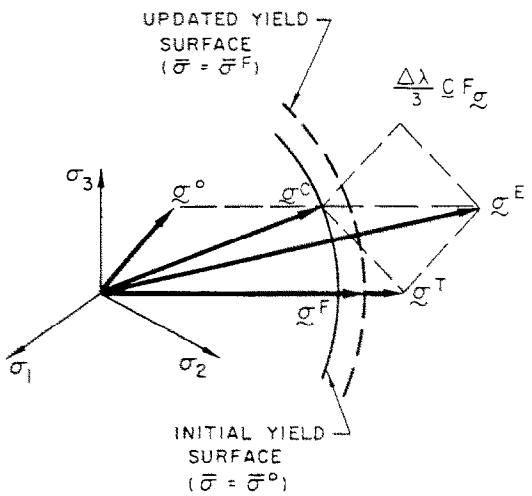

FIG. 23. Stress computation in the finite element scheme based on an explicit integration of the incremental constitutive law.

If convergence is *not achieved*, control is returned to Step (2) to perform the next iteration. If convergence is *achieved*, control is returned to Step (1) to perform the next time step.

Explicit integration of incremental constitutive law

The method of stress computation mentioned in Section 2 is outlined for an isotropic hardening solid below.

(1) After solving the finite element equilibrium equations for the nodal displacement increments $\Delta\mathbf{U}$, the strain increment $\Delta\boldsymbol{\varepsilon}$ is obtained as

$$\Delta\boldsymbol{\varepsilon} = \mathbf{B}\Delta\mathbf{U},$$

where $\mathbf{B}$ is the strain-displacement matrix.

(2) An elastic estimate $\Delta\boldsymbol{\sigma}^E$ for the stress increment is computed as

$$\Delta\boldsymbol{\sigma}^E = \mathbf{C}\Delta\boldsymbol{\varepsilon}.$$

(3) A trial stress state $\boldsymbol{\sigma}^E = \boldsymbol{\sigma}^0 + \Delta\boldsymbol{\sigma}^E$ is calculated from the stress state $\boldsymbol{\sigma}^0$ at the beginning of the iteration. Here $\boldsymbol{\sigma}^0$ is taken to be inside the yield surface (Fig. 23) for the sake of definiteness.

(4) If $F(\boldsymbol{\sigma}^E) - (\bar{\sigma}^0)^2 \leqslant 0$, where $\bar{\sigma}^0$ is the value of $\bar{\sigma}$ at the beginning of the iteration, then the elastic behaviour assumption holds and the remaining steps in this method are omitted. Otherwise, the yield surface has been crossed during the trial stress incrementation (Fig. 23).

(5) The contact stress state $\boldsymbol{\sigma}^C$ is obtained as

$$\boldsymbol{\sigma}^C = \boldsymbol{\sigma}^0 + q\Delta\boldsymbol{\sigma}^E,$$

where $0 \leqslant q < 1$ and $F(\boldsymbol{\sigma}^C) - (\bar{\sigma}^0)^2 = 0$. This condition for the Von Mises yield function leads to a quadratic equation in q. It should be observed that the path from $\boldsymbol{\sigma}^0$ to $\boldsymbol{\sigma}^C$ constitutes fully elastic material response.

(6) A stress state $\boldsymbol{\sigma}^T$ is obtained as

$$\boldsymbol{\sigma}^T = \boldsymbol{\sigma}^C + \mathbf{C}\left((1-q)\Delta\boldsymbol{\varepsilon} - \frac{\Delta\lambda}{3}F_\sigma\right)$$

$$= \boldsymbol{\sigma}^C + \left((\boldsymbol{\sigma}^E - \boldsymbol{\sigma}^C) - \frac{\Delta\lambda}{3}\mathbf{C}F_\sigma\right).$$

In this equation, F_σ is taken as the normal to the yield surface at the stress state $\boldsymbol{\sigma}^C$. Also, $\Delta\lambda$ is evaluated corresponding to the stress state $\boldsymbol{\sigma}^C$.

(7) The yield surface is updated as

$$\bar{\sigma}^F = \bar{\sigma}^0 + H(\bar{\sigma}^0)\Delta\bar{\varepsilon}^p,$$

where

$$\Delta\bar{\varepsilon}^p = \tfrac{2}{3}\Delta\lambda\bar{\sigma}^0 \quad \text{and} \quad H(\bar{\sigma}^0) = \left.\frac{d\bar{\sigma}}{d\bar{\varepsilon}^p}\right|_{\bar{\sigma}^0},$$

which can be obtained from (2.4) for hardening solids and is set equal to zero for perfect plasticity.

(8) Due to the finite nature of the time step, the stress state $\boldsymbol{\sigma}^T$ obtained in Step (6) will not (in general) lie on the updated yield surface. $\boldsymbol{\sigma}^T$ is then simply scaled as follows,

$$\boldsymbol{\sigma}^F = \left(\frac{\bar{\sigma}^F}{\sqrt{\tfrac{3}{2}S_{ij}^T S_{ij}^T}}\right)\boldsymbol{\sigma}^T.$$

The path from $\boldsymbol{\sigma}^C$ to $\boldsymbol{\sigma}^F$ constitutes elastic–plastic material response. In order to minimize the error due to the use of finite increments, the excess stress $\boldsymbol{\sigma}^E - \boldsymbol{\sigma}^C$ is divided into m subincrements, and Steps (6) to (8) are carried out m times with the subincrements.